

VERIFICATION OF DIRECT BRACHYTHERAPY DOSIMETRY
FOR A SINGLE SEED IMPLANT

A Thesis

Submitted to the Graduate Faculty of
Louisiana State University and
Agricultural & Mechanical College
in partial fulfillment of the
requirements for the degree of
Master of Science

in

The Department of Physics and Astronomy

By
Jabari Robinson
B.S., Southern University and A&M College, 2003
December 2006

TABLE OF CONTENTS

LIST OF FIGURES	iii
ABSTRACT	v
CHAPTER 1. INTRODUCTION	1
1.1 Objective of the Thesis	2
1.1.1 Specific Aims.....	3
1.2 Organization of the Thesis.....	4
1.2.1 Methods.....	4
CHAPTER 2. BACKGROUND AND SIGNIFICANCE.....	6
2.1 Background on Prostate Cancer.....	6
2.2 Background on Breast Cancer	10
2.3 Current Brachytherapy Seed Dosimetry	12
CHAPTER 3. EXPERIMENTAL.....	14
3.1 Characteristics of Experimental Seeds.....	14
3.2 PET/CT Scans.....	16
3.2.1 Data Extraction from the PET Images	17
3.2.2 PET Acquisition Protocols.....	18
CHAPTER 4. COMPUTATIONAL.....	21
4.1 Computation of D_t Using MCNP Based on Measured PET Data.....	21
4.1.1 Data Types and Computation of Inverse Matrices	21
4.1.2 Tally Types of MCNP Suitable for This Project	24
4.1.3 Data Analysis.....	28
CHAPTER 5. RESULTS.....	30
5.1 Seed in Prostate.....	30
5.2 PET Intensity Redistribution to Improve Results	33
5.3 Seed in Breast	34
5.4 Analysis of Results	37
CHAPTER 6. SUMMARY.....	42
REFERENCES	45
APPENDIX A. SAMPLE MCNP INPUT FILE.....	48
APPENDIX B. IDL DATA EXTRACTION PROGRAM FOR DICOM.....	51
APPENDIX C. SAMPLE MAPLE PROGRAM FOR THE SW METHOD	53
VITA.....	65

LIST OF FIGURES

1. Geometry of a Theraseed™ Pd-103 seed	2
2. Schematic of Prostate Seed Implant Procedure	7
3. Front View of Template.....	8
4. Side View of Template in Operation	8
5. Mammosite Balloon and Catheter	11
6a. Flattened MammoSite Balloon with Catheter.....	12
6b. Inflated Balloon	12
6c. Radioactive Seed Attached to a Wire.....	12
6d. Deflated Balloon	12
7. Isodose Contour for a Breast Implant	12
8. Palladium-103 Seeds.....	14
9. Acrylic Phantom with Holes to Hold Seeds	17
10. Streaking for FBP vs. OSEM.....	19
11. Dose Comparison of Tally Types	28
12. Dose Comparison for the Prostate Case.....	31
13. Ratio of Doses versus Benchmark Computation for Prostate Case.....	32
14. Discrepancy Comparison of Variable Percentage vs. 100 Percent in the Breast.....	34
15. Half-sphere (semi-infinite medium) vs. Full-sphere (infinite medium) Dose Comparison at 4 mm from the Transverse Axis of the Seed.....	35
16. Half-sphere vs. Full-sphere Dose Contours	35
17. Calculated Radial Dose Function for Ir-192.....	36
18. Dose Comparison for the Breast Case	37

19. Discrepancy Comparison for Using only *f8 Tallies vs. Combined *f8 and f6.....	38
20a. Idealized Geometry with a Single Voxel Source	39
20b. Idealized Geometry with Blurred Source	39
21. Kerma Comparison of Ideal vs. Blurred.....	40
22. Discrepancy in Dose Using Idealized vs. Blurred PET Image	41

ABSTRACT

A new technique using direct post-implant dosimetry, which does not depend explicitly on brachytherapy seed orientation or position, was explored for a prostate and a breast case. This technique, proposed by E Sajo and ML Williams (SW), uses trace amounts of positron emitters placed in the seed capsule and uses the positron emission tomography image in conjunction with a computed tomography image (PET-CT) to compute the therapeutic dose distribution in the patient. The SW technique could reduce errors in the post-implant dose computations associated with seed localization, seed shadowing and medium heterogeneity. Dose point kernels were obtained using Monte Carlo simulation for a single seed in a breast and prostate geometry. Green's functions were computed for the positron marker and therapeutic photons using Monte Carlo (MC) simulations. Various dose computation options in the MC code MCNP were compared and the best were selected for this project. A single seed was imaged for a prostate phantom and a breast phantom using a PET-CT. The image data was used to obtain dose for the annihilation photons for the experimental seeds. The Sajo-Williams mathematical method was used to compute the therapeutic dose of the seed based on the positron marker dose. The therapeutic dose computed this way was compared to the dose obtained using the Pinnacle³ treatment planning software and to an MCNP benchmark model. For the breast case the comparison showed a good agreement with Pinnacle³, but both under-predicted the dose close to the source with respect to the benchmark. For the prostate case Pinnacle³ somewhat under-predicted the values in the MCNP benchmark, and the SW method appreciably under-predicted the dose near the source. In all cases, farther away from the source where most of the dosimetric interests lie, the agreement is very good.

CHAPTER 1

INTRODUCTION

The work in this thesis is concerned with a new dosimetry method proposed in the brachytherapy of the prostate, with possible applications to the breast as well.

Brachytherapy is a method of treatment in which sealed radioactive sources are used to deliver radiation dose at a short distance by interstitial, intracavitary, or surface application. With this mode of therapy, a high radiation dose can be delivered locally to the tumor with rapid dose fall-off in the surrounding normal tissue (F. Khan, p.357).

There are two types of prostate brachytherapy: temporary and permanent implants.

Permanent implants utilize small needle-like sources, called seeds, and are the more popular and widely used of the two. Permanent implants are used in treatment of early stage prostate cancer. Iodine-125 and palladium-103 are commonly used radio-isotopes for permanent seed implants. Figure 1 shows the schematic drawing of a prostate seed. In the schematic, 1 is the titanium encapsulation of the seed, 2 is a radio-opaque marker, and 3 represents the palladium-103 plated graphite pellets. Usually, implanted seed positions deviate from the pattern developed in treatment planning, because of source positioning errors due to inaccurate needle placement, prostate motion, and seed splaying.

Postoperative assessment of patient outcome relies on seed localization and orientation.

Errors in seed localization contribute to uncertainty in the amount and distribution of delivered dose. Also, once the seed location are known, the computation of the dose distribution relies on a point source algorithm which neglects anisotropy, medium heterogeneity, and seed shadowing effects in target regions.

1.1 Objective of the Thesis

A new technique using direct post-implant dosimetry, which does not depend explicitly on seed orientation or position, was recently proposed (Sajo and Williams, 2004). This method could eliminate some of the errors in the dose computations associated with seed localization, seed shadowing and medium heterogeneity while accelerating the process of dosimetry. This technique uses a positron emitter in tracer quantities inside the seed capsule. The dose due to the annihilation photons can be obtained by the observations using PET/CT. Subsequently,

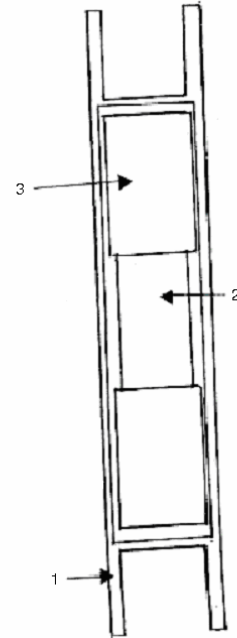


Figure 1-Geometry of a Theraseed™ Pd-103 seed.

the therapeutic dose may be calculated from the annihilation dose, as described in the third section of this thesis. The activity of the positron marker isotope is a fraction of the activity of the therapeutic isotope. The radiation dose of the marker isotope delivered beyond the immediate vicinity of the seed is low because the marker isotope is adapted to have an activity of an order of magnitude lower than the activity of the therapeutic isotope. Therefore the presence of the marker isotope should not alter the therapeutic characteristics of the seed.

Dose computation based on the observed annihilation dose entails use of therapeutic and positron Green's functions to scale the positron dose in Fourier space which gives the therapeutic dose in Fourier space. The objective of this thesis is to verify that for one seed the proposed technique (Sajo and Williams, 2004) works. This entailed both experimental and computational work, as outlined here.

1.1.1 Specific Aims

- I. Obtain dose point kernels using Monte Carlo simulation for a single seed in a breast and prostate geometry.
 1. Find the Green's function for the positron marker dose.
 2. Find the Green's function for therapeutic photons.
 3. Compare various dose computation options in MCNP, including the integral point kernels using ICRP response functions, and select the best method for tallying the dose.
- II. Image one simulated seed in a prostate phantom and another one in a breast phantom using PET/CT.
 1. Save the PET data and extract the annihilation intensity information.
 2. Obtain the dose for the annihilation photons using PET data according to reference (Jarrett and Sajo, 2005).
- III. Compute the therapeutic dose of the seed based on the positron marker dose obtained in II.1 using the mathematical method as described in reference (Sajo and Williams, 2004).
- IV. Compute the therapeutic dose using the Pinnacle treatment planning software based on traditional localization, obtained in II.2.
- V. Compute the therapeutic dose distribution based on a previously assumed therapeutic activity and on the actual seed geometry and position using Monte Carlo radiation transport simulation. This will be used as benchmark.

- VI. Compare results obtained in aims III, IV, and V at various distances and angles from the seed.

1.2 Organization of the Thesis

1.2.1 Methods

Computational:

The mathematical fundamentals of the method described in (Sajo and Williams, 2004) and are outlined in Chapter 4. The numerical technique used in this study is also explained there, along with some of the fundamentals of the Monte Carlo simulation method. The computations entailed three types of simulation: (1) a benchmark run to compute the therapeutic and positron doses where the precise seed geometry with known source energies and distributions were modeled, (2) simulation of the seeds (for prostate and breast) to obtain the Green's function kernels, (3) computation of the PET dose based on measured annihilation event distribution using simulated radioactive seeds in a prostate phantom. The mathematical method, as explained in chapter 4, requires data obtained in (2) and (3). The resulting therapeutic dose is compared to the benchmark MC run (1).

Experimental:

The experiments entailed imaging a simulated seed in acrylic prostate and breast phantoms using a PET/CT. The seeds were manufactured using a hollow needle filled with a positron emitter radioisotope and crimped at both ends. The needle diameter and capsule wall thickness were selected to conform to most typical brachytherapy seeds. One to three microcuries of Na-22 isotope was placed inside the seeds before sealing them. Because the endpoint energy of Na-22 positrons is 0.545 MeV and their average

energy is 0.215 MeV, their range in the stainless steel seed encapsulation is shorter than the wall thickness. Therefore, all annihilations will take place inside the seed.

The PET images were subsequently analyzed and pixel-wise activities were extracted. These activities represent the detected annihilation events in the pixels. The resolution of the images, the effect of false counts, and other details will be discussed in Chapter 3. A background on traditional brachytherapy of the breast and prostate and dosimetry is given in chapter 2.

CHAPTER 2

BACKGROUND AND SIGNIFICANCE

2.1 Background on Prostate Cancer

The highest incidence of cancer in males in the United States (excluding skin cancer) is prostate cancer. It also has the second highest mortality rate in men. In recent years the use of permanent interstitial implants for treating prostate cancer has increased. The reason for this is improvements in diagnosis at the early stage of the disease as well as refinements in the brachytherapy technique. Permanent implants with iodine-125 or palladium-103 are used in the treatment of early stage prostate cancer as the sole modality or in combination with external beam radiation therapy. The target volume for implantation in either case is the prostate gland itself, with minimal margins allowed to account for uncertainty of prostate localization. The modern technique of implantation, which began in the 1980s, consists of transperineal approach in which iodine-125 or palladium-103 seeds are inserted into the prostate gland with the guidance of transrectal ultrasonography and perineal template (Figure 2). When using permanent interstitial implants, the dose distribution depends on the accuracy of the source positioning with respect to the treatment plan. Post-implant analysis describes how the actual dose distribution conforms to the desired dose.

There are organized steps in prostate brachytherapy that ensures the efficiency and accuracy of the process. These steps include the volume study, the treatment planning stage, the implant procedure, and the post-operative analysis. The volume study is the pre-planning stage, in which the size of the important structures is identified. The

post-operative analysis is when the actual dose distribution is compared to the planned one.

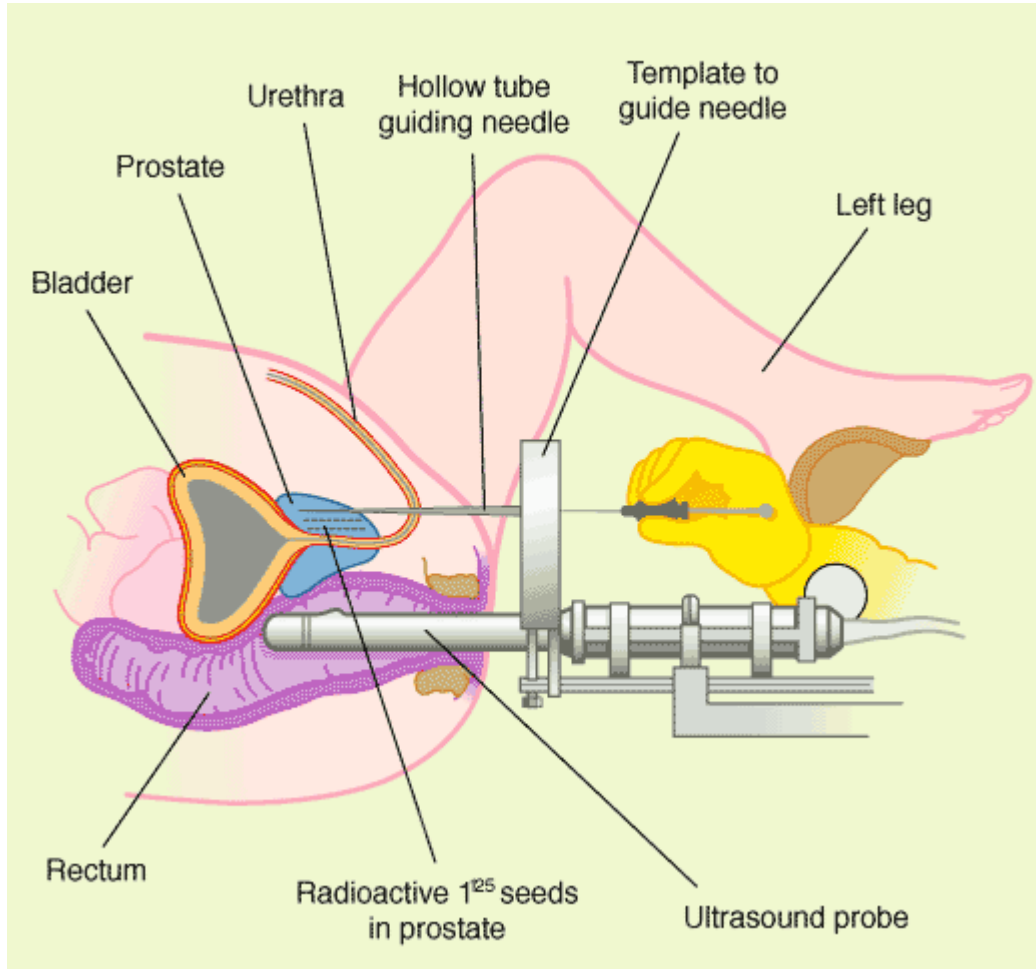


Figure 2-Schematic of Prostate Seed Implant Procedure

The volume study is one of the first steps in prostate implants. It is the localization of the prostate by a series of transverse ultrasound images. CT scans are done to determine the size of the prostate gland and pubic arch. If the gland is too large and the pubic arch is too narrow then hormonal therapy may have to be done before prostate seed implantation can be a viable treatment option. A transrectal ultrasound probe is used to acquire transverse images of the prostate gland at intervals of about 5mm. A grid is

placed on these images, which represents template coordinates. The template is the physical grid that is placed on the patient to guide needles to the proper position.



Figure 3-Front View of Template

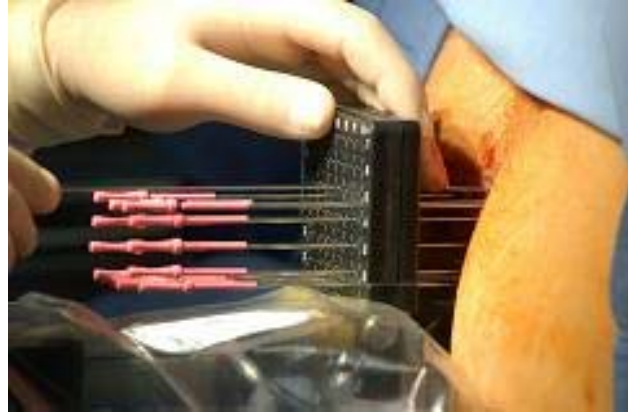


Figure 4-Side View of Template in Operation

The prostate is visualized and drawn on each image. To measure the length of the prostate a sagittal image is taken.

Target outlines from the volume study are digitized into a computer using treatment-planning software. The planning software is used to place seeds in the template grid throughout the ultrasound images. In the software, seeds can be added or deleted as necessary to obtain an acceptable dose to volume coverage. Also, the source strength can be modified, but only one source strength is used for all seeds. When the plan is complete a worksheet is printed that provides the number of needles, seeds in the needles, and the coordinates of the needles.

The prostate implant procedure is a nonsurgical procedure performed on an outpatient basis. It is done in an operating room with the patient under anesthesia. A transrectal ultrasound and a transperineal template are used to guide seed containing needles into position, as shown in Figure 2. The needles are preloaded with the planned number of seeds and spacers and the tip is sealed with bone wax. By using the ultrasound

images and distance measurements from the hub of the needle to the template the needle tip is positioned to the correct plane and depth. Afterwards, the needle is withdrawn while the plunger is held stationary. Thus the seeds and spacers are injected into the tissue along the track of the withdrawing needle. The implant is verified using anterior-posterior fluoroscopy. If any cold spots are identified extra seeds are available.

Post-implant analysis relies on knowledge of seed location, knowledge of seed orientation, and the resolution of the imaging device. The seed locations and orientations are extracted from the post-implant imaging study, and the dose distribution in the prostate is then computed and compared to the treatment plan. Despite increasingly sophisticated mathematical methods, accuracy of the dose reconstruction algorithms is still hindered by undesirable uncertainties. For example, in phantom studies, orthogonal film reconstruction techniques can locate only 66% of the seeds within 5 mm of their actual location (Bice et al, 1999; Tubic et al, 2001). Recent efforts using CT-based localization show improved accuracy in determining the positions of seeds, but the detection of the orientations of overlapping seeds are still only rough estimates. Also, although the seed orientation can be input to the post-plan software, only one seed orientation will be used for all seeds throughout the computations. Some additional problems are artifacts in the images and difficulties with localizing seeds across multiple CT images. Since low energy photon emitters, such as Pd-103 and I-125, are used in prostate seeds, the uncertainty in the estimated dose due to localization errors of only a few millimeters can be significant due to the sharp dose rate falloff.

Also, most dose computation methods in use do not take into account seed shadowing effects and the fact that the tissue composition of the prostate is not water-

equivalent. Recent studies indicate that the seed shadowing effect, when correctly computed, can amount to a 3% to 5% discrepancy from the case when the individually computed doses are superimposed (Yegin and Rogers, 2004; Carrier, 2006). When the prostate tissue composition is also taken into account, the total discrepancy from water-based dose computations using the superposition technique is up to about 13% (Carrier, 2006). Additional confounding factors, such as heterogeneities in prostate composition, which is due to post-implant edema and needle traces, further increase the discrepancy between the traditionally computed doses, using for example the AAPM Task Group Report 43 method (Nath et al, 1995; Rivard et al, 2004), and the correctly computed doses using rigorous radiation transport methods (Jarrett and Sajo, 2005).

2.2 Background on Breast Cancer

Just as prostate cancer has the highest incidence of all cancers in males; breast cancer has the highest incidence of all cancers in women (excluding skin cancer). With better screening, the number of incidences has increased in recent years; there were over 178,000 cases in 1998. After removing a breast tumor with surgery, irradiating the tumor bed is often done. One method of irradiating the tumor bed is by using external beam 3D conformal radiation therapy. The other method, in the case of lumpectomy, is by using breast brachytherapy. A new and minimally invasive means of brachytherapy for partial breast irradiation is the MammoSite HDR Brachytherapy System (the MammoSite catheter is shown in figure 5).

The treatment is given on an outpatient basis. A flattened MammoSite balloon with catheter is inserted into the tumor resection cavity (figure 6a). Once in place, the

balloon is inflated with saline and a contrast agent (figure 6b). A CT scan is taken and a treatment plan is developed after waiting a day for edema to occur. After the balloon

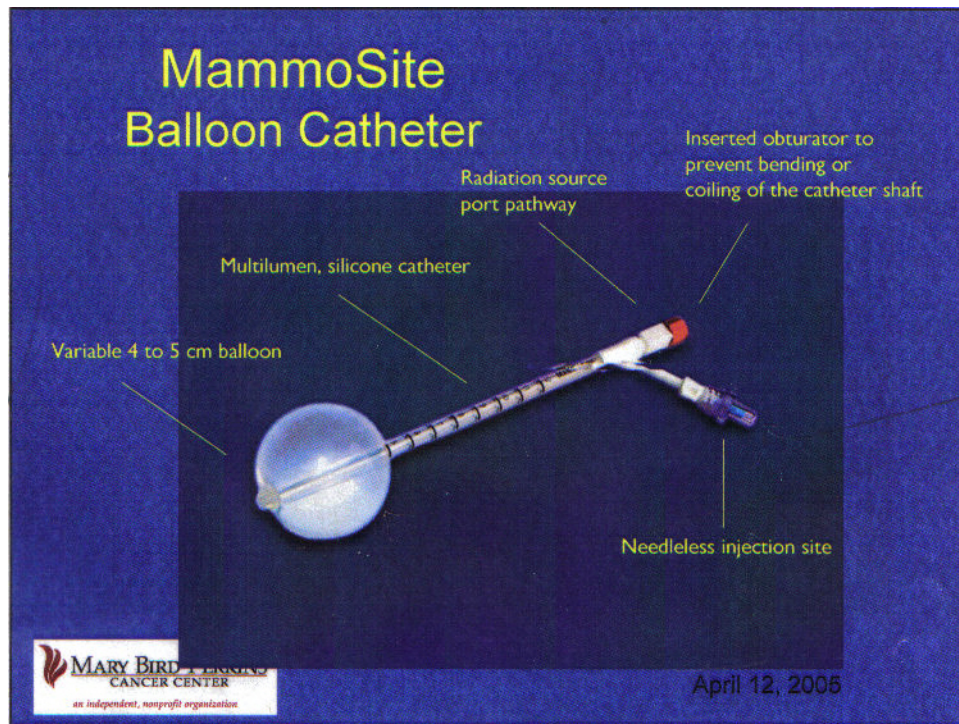
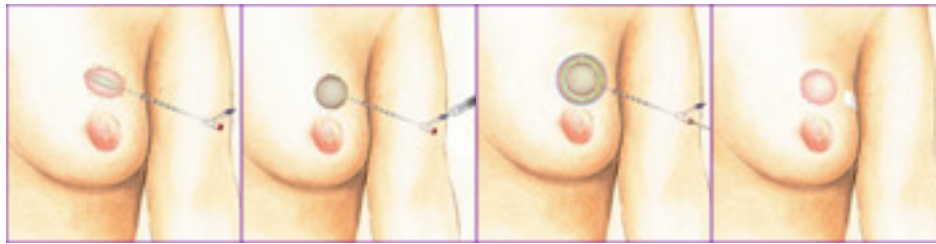


Figure 5-Mammosite Balloon and Catheter

integrity and constancy is conformed treatment can begin. A radioactive seed attached to a wire delivers dose to the patient (figure 6c). After treatment the balloon is deflated and removed along with the catheter (figure 6d). The dosimetry for Mammosite HDR is based on TG-43 (Nath et al, 1995; Rivard et al, 2004), which assumes an infinite homogeneous medium. Because of heterogeneity issues, especially at the skin-air interface, there is a discrepancy in the dosimetry. This is illustrated in figure 7 where a continuous isodose curve is seen as it goes in the air region, as though it was still tissue (courtesy of Mark Rivard, Tufts University Medical Center, Boston, MA. Personal communication, 2006). This raises the possibility that the dosimetry method described herein may be applicable to breast brachytherapy as well.



(a) (b) (c) (d)

Figure 6-(a) Flattened MammoSite Balloon with Catheter; (b) Inflated Balloon; (c) Radioactive Seed Attached to a Wire; (d) Deflated Balloon

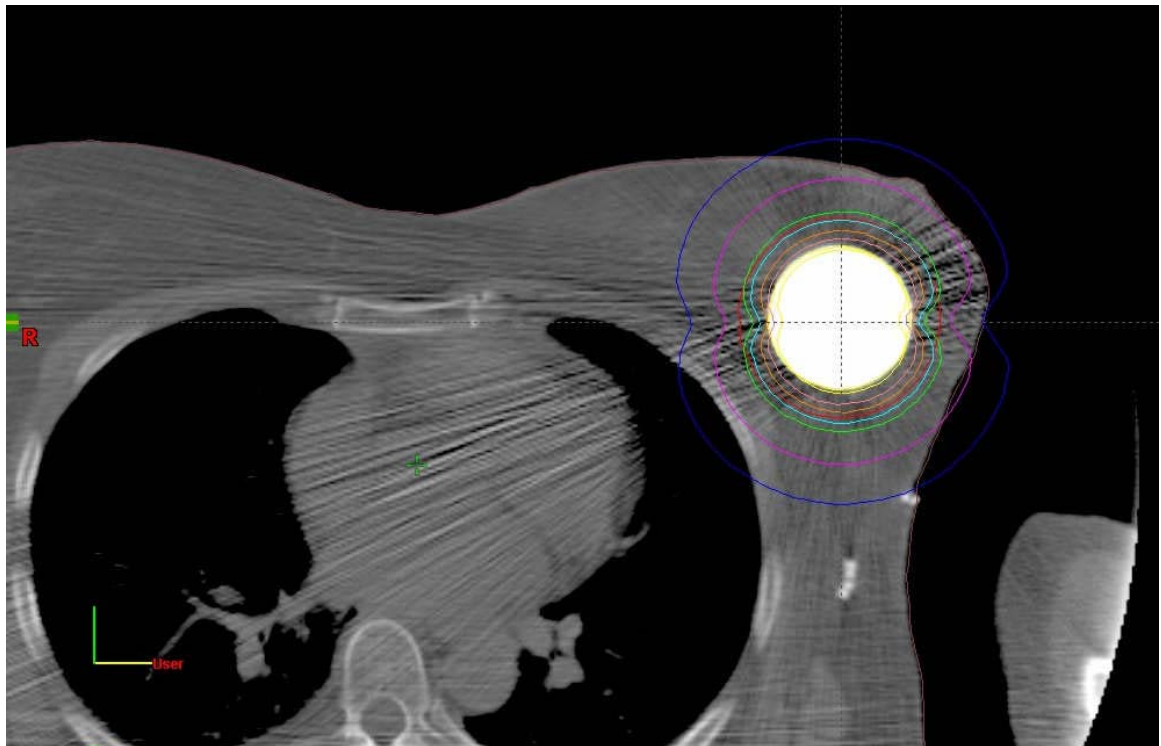


Figure 7-Isodose Contour for a Breast Implant

2.3 Current Brachytherapy Seed Dosimetry

In 1988 the Radiation Therapy Committee of the American Association of Physicists in Medicine (AAPM) formed Task Group No. 43 to review the publications on the dosimetry of interstitial brachytherapy sources and recommend a dosimetry protocol which would include formalism for dose calculations and a data set for the values of the dosimetry parameters for a few commonly used seed types. Since the publication of TG-

43 in 1995 (Nath et al, 1995), both the utilization of the permanent source implantation and the number of low-energy interstitial brachytherapy source models commercially available have dramatically increased. Additionally, the National Institute of Standards and Technology introduced a new primary standard of air-kerma strength, and the brachytherapy dosimetry literature grew greatly, documenting both the improved dosimetry methodologies and dosimetric characterization of particular source models. Therefore, in February of 2004 an update to TG-43 was published (Rivard et al, 2004). The update to TG-43 included: a revised definition of air-kerma strength; elimination of apparent activity for specification of source strength; elimination of the anisotropy constant in favor of the distance-dependant one-dimensional anisotropy function; guidance on extrapolating tabulated TG-43 parameters to longer and shorter distances; and correction for minor inconsistencies and omissions in the original protocol and its implementations. Despite the advancements introduced in TG-43 and its update, there are still problems that affect the computed dose. TG-43 assumes an infinite homogenous medium for calculating dose. Also, it does not account for attenuation from other seeds in the medium.

CHAPTER 3

EXPERIMENTAL

3.1 Characteristics of Experimental Seeds

There were two experimental seeds that were used in this project, both attempted to approximate the physical dimensions of commercially available seeds. Typical dimensions of a prostate seed is 4.5 mm length and 0.8 mm diameter with an encapsulation wall thickness of about 0.1 mm. Figure 8 shows palladium-103 seeds manufactured by TheraSeed. Brachytherapy seeds for a mammosite implant are typically between 2-4 mm in length and less than 1 mm in diameter. In the breast implant a source train of several iridium-192 seeds is used.

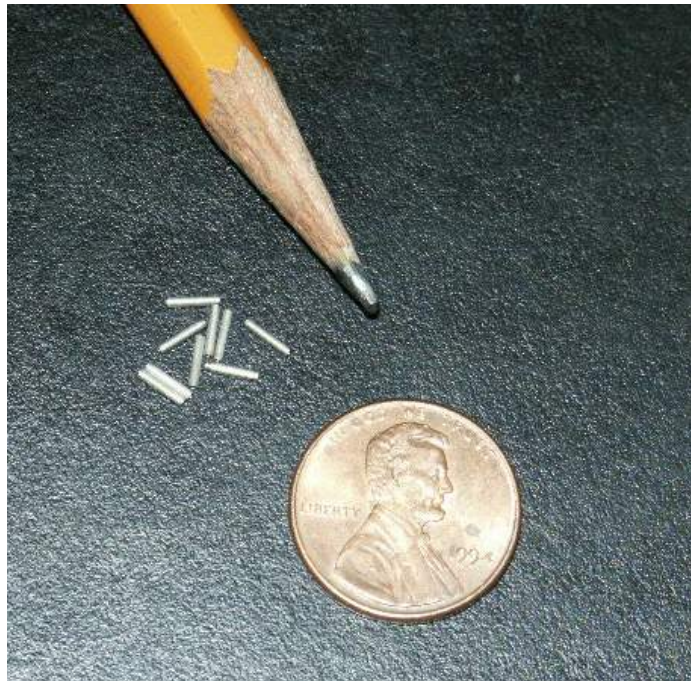


Figure 8-Palladium-103 Seeds

Most seeds are encapsulated in titanium.

One of the simulated seeds was used in the prostate phantom and one was used in the breast phantom. Both of the seeds were made from stainless steel needles with crimped ends. Because all positrons are expected to annihilate in the seed capsule, even when it is made of titanium, steel is a good surrogate to this end. A B-D 22 gauge needle was used to construct the prostate seed. The prostate seed was filled with a FDG (fluorine-18) solution. Fluorine-18 has a half-life of 1.8 hours and a maximum positron

energy of 645 keV and average positron energy of 250 keV (yield of 97%). The breast seed was filled with a solution containing sodium-22. Sodium-22 has a half-life of 2.6 years, maximum positron energy of 546 keV and average positron energy of 215 keV (yield of 89.8%). In addition to positron emission, sodium-22 emits also gamma photons with an energy of 1275 keV (yield of 99.94%). Since no information on the wall thickness was available from B-D and since the manufacturer of the needle used in the breast case is unknown, a Skyscan micro CT (model 1074) was used to find the wall thicknesses of both seeds. The micro CT has a field of view of about 4 cm and resolution of 37 μm . The approximate length of the prostate seed was 5.2 mm. The diameter was about 0.66 mm with a 0.2 mm wall thickness. The length of the breast seed was 1 cm and the diameter was 1.14 mm. The thickness of the seed wall varied azimuthally from 0.1 to 0.2 mm making an average of 0.15 mm.

In conventional PET imaging, where FDG in normal form is injected in the patient, the positron range is partially responsible for blurring of a reconstructed (PET) image. In our case, however, the positron emitter is encapsulated and thus the range blurring is either eliminated or at least substantially reduced in our experiments. Positron range is one of the main factors that limit the spatial resolution of PET images. A positron travels a small distance before it annihilates with an electron. The length of this distance, positron range, depends on the energy of the positron and the atomic number or electron density of the medium it traverses. Using continuous slowing down approximation (CSDA) the positron ranges for Na-22 and F-18 can be calculated. ICRU Report 37 lists these parameters for most materials of interest. Table 1 lists the positron

energies and their respective ranges in water and iron, the materials of interest in our experiments.

Table 1. Positron Ranges for Na-22 and F-18

	Energy (keV)	Λ_{water} (mm)	Λ_{Fe} (mm)
Na-22			
Endpoint	545	2.0	0.38
Mean	215	0.45	0.09
F-18			
Endpoint	635	2.5	0.45
Mean	250	0.62	0.12

3.2 PET/CT Scans

The prostate seed was placed in the center of an acrylic phantom 4 cm in length, 4 cm in width, and 3 cm thick. The breast seed was put in the center of a 1.5 cm piece of acrylic that was put on top of the prostate phantom.

A General Electric (GE) PET/CT scanner was used in this project. Positioning lasers were used to align the seed in the phantom with the center of the CT image. A scout scan was done to produce an x-ray image of the seed and phantom. This image was used to determine the axial examination range. After defining that range the CT/PET couch moved the phantom to the CT field of view for the CT scan. After the CT scan was complete the couch moved the phantom into the PET field of view for the PET scan. Then reconstruction was done with attenuation correction and the data was saved to a compact disc.

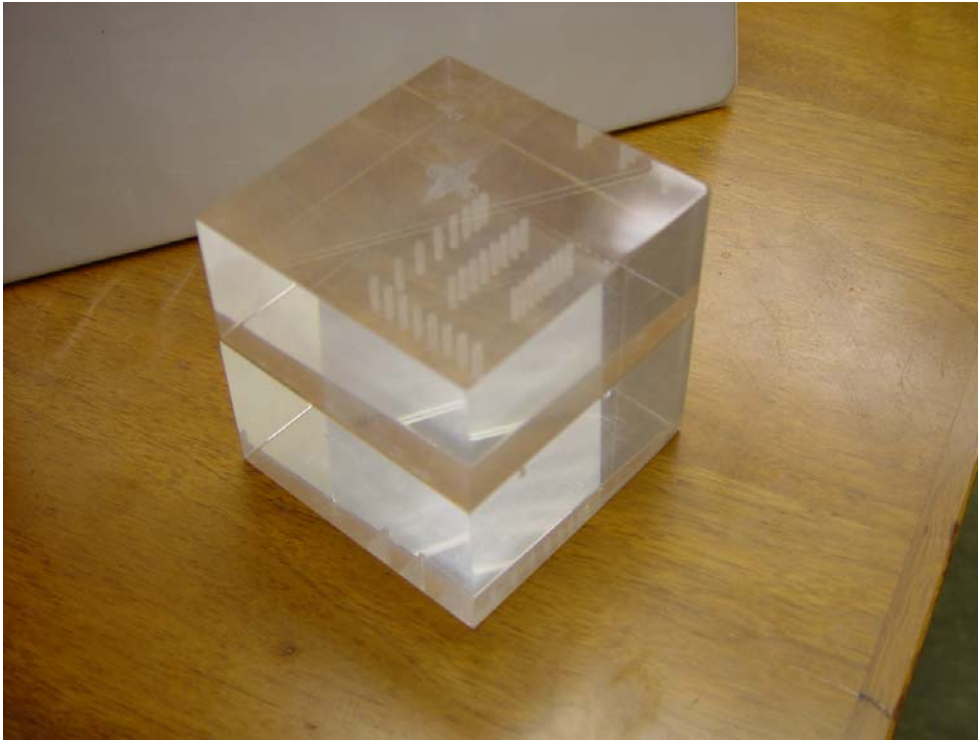


Figure 9-Acrylic Phantom with Holes to Hold Seeds.

3.2.1 Data Extraction from the PET Images

Positron emission tomography works by detecting annihilation photons from a positron source. As discussed earlier, a positron travels a small distance, the range, and then annihilates with an electron producing two 511 keV photons that are emitted in opposite directions. The ring detector of the PET machine detects these photons using coincidence counting and registers the photons detected opposite to each other using straight lines to determine the origin of annihilation events. PET scans are used primarily for qualitative means rather than quantitative. Therefore, this is reflected in the software that reconstructs the PET image. For the purpose of this project we needed quantitative analysis. We relied on the information given in the image files (often referred to as DICOM files, because it uses this National Electrical Manufacturers Association-NEMA standard) to extract pixel intensity values. To ensure uniform brightness across many

images, the pixel intensity values of each image are automatically rescaled. The rescale values are reported in the DICOM files. IDL programming language was used to get pixel information including length, width, and thickness. The voxel dimensions were 0.585 by 0.585 by 3.27 mm. IDL was used to eliminate rescaling and to get the original pixel intensity values at and around the seed region. It was difficult to identify the values that correspond to the region of the seed for the breast case, because there were a few high false counts throughout the field of view. A commercially available program, called OSIRIS, was used to help locate the position of the seed. PET scans give a blurred extra region of space around the area of actual positron concentration. Some of the intensity that belongs in the seed region is in this blurred region. By fitting a Gaussian curve in the x, y, and z directions, the center of the seed was located, as defined by its peak centroid. By using the Gaussian curves the full width at half maximum (fwhm) in each direction was obtained. By using the fwhm the values for the standard deviation, sigma, was acquired. $3 \times \text{sigma}$ (which includes 99.75% of the Gaussian) was considered to be the maximum distance away from the center that contributes to the intensity of the seed region. It was assumed that activity detected beyond $\pm 3\sigma$ were not due to the seed activity.

3.2.2 PET Acquisition Protocols

There are various protocols in the PET software that give varying degrees of spatial resolution. Some of the parameters which affect spatial resolution included field of view (FOV), acquisition time, and reconstruction method. The parameters that were used in this project were the parameters that were best for the one seed case. Those parameters were 4-minute acquisition, 15 cm field of view, 256 by 256 resolution, and a

method of reconstruction called Ordered Subset Expectation Maximization (OSEM). Expectation Maximization is an algorithm for finding the maximum likelihood of parameters in probabilistic models where the model depends on unobserved latent variables. Expectation optimization alternates between performing an expectation (E) step, which computes an expectation of the likelihood by including the latent variables as if they were observed, and a maximization (M) step, which computes the maximum likelihood estimates of the parameters by maximizing the expected likelihood found on the E step. The parameters found on the M step are then used to begin another E step, and the process is repeated. OSEM gives better noise ratios and eliminates the streaking that is found in the Filtered Backprojection (FBP) method.

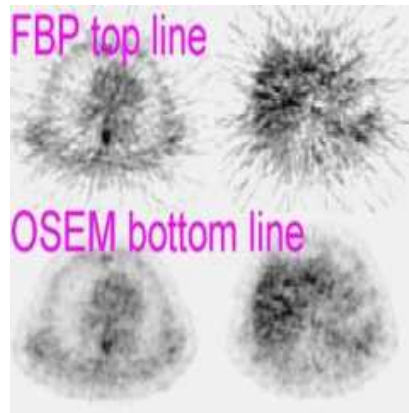


Figure 10-Streaking for FBP vs. OSEM

Filtered Backprojection uses Fourier theory to arrive at a closed form solution to the problem of finding the linear attenuation coefficient at various points in the cross section of an object. Since it is filtered backprojection the data is filtered while in the frequency domain. In the backprojection phase the bin data from the filtered sinogram is smeared back along the same lines from where the photons were emitted from. Areas

where the backprojection lines from different angles converge represents areas which contains higher concentration of radiopharmaceutical.

CHAPTER 4

COMPUTATIONAL

4.1 Computation of Dt Using MCNP Based on Measured PET Data

4.1.1 Data Types and Computation of Inverse Matrices

Along with the new dosimetry technique, a mathematical method was developed to link the therapeutic dose distribution to the positron annihilation event distribution (Sajo and Williams, 2004). Monte Carlo calculations and PET imaging can be used to verify this mathematical method for a few seeds, before a full computational algorithm is developed for an array of seeds. The details of the mathematical method are described in the original paper (Sajo and Williams, 2004), however the main idea can be expressed by focusing on the last steps. The dose deposited by the positrons may be written as

$$D_p(d) = \frac{1}{V_d} \int dV_s \int dV_d S_v(\bar{r}_s) G_p(\bar{r}_s, \bar{r}_d), \quad (1)$$

where V_d is the volume of the detector, V_s is the volume of the source, r_s is the position of the particle at the source, r_d is the position of the particle at the detector, G_p is the point kernel for the positron emitter, and S_v is the volumetric source. The dose due to the therapeutic isotope is written similarly:

$$D_T(d) = \frac{1}{V_d} \int dV_s \int dV_d S_v(\bar{r}_s) G_T(\bar{r}_s, \bar{r}_d) \quad (2)$$

Fourier transform of equations 1 and 2 gives $V_d \tilde{D}_p = \tilde{G}_p \cdot \tilde{S}_v$ and $V_d \tilde{D}_T = \tilde{G}_T \cdot \tilde{S}_v$,

respectively. Because the dose volumes are identical, if the location of the two sources, therapeutic and positron, are coincident, division of the two equation yields the therapeutic dose as function of the positron dose:

$$\tilde{D}_T = \tilde{G}_T \cdot \tilde{G}_p^{-1} \cdot \tilde{D}_p, \quad (3)$$

where \tilde{D}_T is the Fourier transform of the therapeutic dose, \tilde{G}_T is the Fourier transform of the point kernel of the therapeutic isotope, \tilde{G}_p the Fourier transform of the point kernel of the positron emitter isotope, and \tilde{D}_p is the Fourier transform of the positron dose.

SW Algorithm for computing the therapeutic dose of seeds based on PET data:

1. Assume that the Green's functions G_p and G_T are point-wise and they may be generated by MC. G_p and G_T represent the Green's functions for the tracer positrons and the therapeutic photons, respectively.

1.a. Find G_p for each pixel, i , in the PET image domain using a pixel-source, j , of 0.511 photons. This will be notated $G_{p, j \rightarrow i}(S_p \rightarrow t)$. The source pixel may contain the entire seed or $1/2$ of the seed, and it is fixed at $j = 1$. Here, the pixels i and j are in the PET coordinate system.

1.b. Find G_T by performing the following:

1.b.1. Obtain the emerging therapeutic photon spectrum from the seed (or $1/2$ seed) with its intensity (i.e. the virtual source) using MC computations.

1.b.2. Assign the virtual source to the same pixel as G_p is assigned to. This will yield $G_{T, j \rightarrow i}(S_T \rightarrow t)$ with j fixed.

2. Measure, using PET, the pixel-wise annihilation events, $\varepsilon_j(j = 1, n)$. PET image gives the intensity of each pixel normalized such as to yield a visible image. This value must be

scaled using the DICOM header information to obtain the true annihilation rate in the pixel, ϵ . This will be the basis for obtaining D_p .

3. Compute $D_{P, j \rightarrow i}$ in a matrix of pixels, i , due to each pixel-source of 0.511 photons in j , using $\epsilon_j (j = 1, n)$ as source. This may be done using:

- MC, using CT pixel-wise HU numbers cross-meshed with the PET pixels.
- directly from PET in the PET coordinate system using attenuation correction by a source whose energy is close to 0.511 MeV.

3.a. If based on MC, sum the contributions from all source pixels, j , to each target pixel, i .

$$D_{P,i}(t) = \sum_{j=1}^n D_{P, j \rightarrow i}(S_P \rightarrow t).$$

The indexes are, $i = 1, m$: target pixel; $j = 1, n$: source pixel.

4. For each pixel, i , compute the Fourier transform of the therapeutic dose:

$$\tilde{D}_{T,i}(t) = \frac{\tilde{G}_{T, j \rightarrow i}(S_T \rightarrow t)}{\tilde{G}_{P, j \rightarrow i}(S_P \rightarrow t)} \tilde{D}_{P,i}(t)$$

The ratio of Fourier transformed Green's functions may be assembled in a look-up table.

Because the last equation entails matrix operation, $\frac{1}{G_{P, j \rightarrow i}(S_P \rightarrow t)} = [G_{P, j \rightarrow i}(S_P \rightarrow t)]^{-1}$,

which is a matrix inverse. In a clinical case it is unlikely that that the matrix

$G_{P, j \rightarrow i}(S_P \rightarrow t)$ will be a square matrix. Thus, the matrix inversion will entail in most

cases a generalized or Moore-Penrose inverse. A Moore-Penrose inverse has the

interesting property that it changes the order of matrix multiplication as function of the

rank of the matrix. When using the generalized inverse of a matrix $[A(n \times m)]$ in which the rank $[R(A)]$ is equal to the number of columns $[m]$ and less than the number of rows $[n]$, then the inverse of the matrix $[A^{-1}]$ is multiplied in the following order: $A^{-1}AA=A$. When $R(A) = n$ and $n < m$ the order of multiplication becomes $AA^{-1}A=A$. For all cases the multiplicative order that gives the best result was used.

Recently, the technology of PET imaging has proliferated. PET image reconstruction however, has problems such as partial volume effect, poor resolution, scatter contribution, system noise, and attenuation correction. To determine the effects of such problems Jarrett (Jarrett and Sajo, 2005) established the possibility and the bounds within which PET data can be used for quantitative dose assessment in support of direct prostate dosimetry. The positron dose calculated by using Monte Carlo simulation was nearly identical to the dose determined based on PET data in cases when there were no large gaps between seeds. In these cases, the error in dose compared to the calculated dose was less than 5 percent.

4.1.2 Tally Types of MCNP Suitable for This Project

MCNP is a general-purpose Monte Carlo N-Particle code that can be used for neutron, photon, electron, or coupled neutron/photon/electron transport. MCNP was used to find the best tally type for geometry similar to the prostate geometry. Since the version of MCNP used in this project does not support positrons as a source a photon source of .511 MeV was placed inside the seed capsule. This is a justifiable approximation because all of the positrons annihilate within the seed. During the course of the project, a new version of MCNP was released which supports positron sources. A comparison run

between the two versions verified that the discrepancy between the computed doses using a positron source versus an annihilation source is marginal.

Tally types for the Green's functions and dose were compared and the best performing tally types were selected. The MCNP geometry was set up according to the dimensions of the prostate seed. MCNP runs were done to obtain therapeutic and positron Green's functions and dose. A mock positron dose was acquired and used in the mathematical method to do a preliminary check. Then the prostate seed was imaged using a GE PET/CT scanner. The image data was saved and the pixel-wise data extracted and manipulated in IDL. True pixel intensity values were obtained at and around the seed region. These values were used in the MCNP input file's source definition to compute the positron dose based on the experimental data, hereinafter referred to as experimental positron dose. Different means of adding contribution from the region outside of the seed were examined. This was necessary because a significant amount of the source that contributes to the dose was outside of the likely source position and a non-negligible fraction of it is false counts due to PET uncertainties. The experimental positron dose was used in the mathematical method to obtain the therapeutic dose and the result was compared to the expected therapeutic dose calculated by MCNP using the known geometry and material compositions. The former may be called "experimental therapeutic dose", while the latter "benchmark therapeutic dose". Also, the experimental therapeutic dose was compared to dose computed by Pinnacle³, a traditional means of calculating brachytherapy dose.

To verify the problem with the breast case, a theoretical half sphere geometry was compared to a large full sphere geometry that mocks an infinite medium. Also, it was

compared to Pinnacle computations near the phantom-air interphase. A modification was made to get a phantom suitable for the breast case. The breast case seed and phantom was imaged and the same process was done as in the prostate case. However, since there were no comparable seeds in the Pinnacle library, MCNP had to be used to compute the radial dose functions for the experimental breast seed for Ir-192 source, which in turn was used in Pinnacle.

The pixel values within the seed region including contribution from the outer region are used as the probability distribution in the source definition of the MCNP input file. Several tally types were investigated in trial runs and it was found that f6 and *f8 were the best tally types to use. The tally types investigated were f4, f5, f6, and f8. Tally type f4 is the track length estimate of cell flux. Track length estimators are used to compute quantities of interest along free streaming trajectories. In the case of the f4 tally the quantity is flux within a cell. Tally type f5 is a next-event estimator, and it can be used to obtain the flux in a point detector or in a ring detector. It was the flux in the ring detector that was investigated. Since both the f4 and the f5 tally give photon flux they had to be multiplied by ICRU response functions to get the energy deposition. The units for f4 and f5 tally are particles/cm². The f6 tally type is the track length estimate of energy deposition over a cell, or kerma. The units for the f6 tally are MeV/g. Tally type f8 is pulse height distribution. The *f8 tally is f8 multiplied by the energy carried by the particles, thus it is an energy deposition tally which accounts for secondary particles as well. The units for the *f8 tally are MeV. The difference between f8 and f6 is that the former gives the dose while the latter gives the kerma. In making comparisons of the tally types the prostate case was used. Speed, relative error, and accuracy were considered

while determining the best tally types. The *f8 tally was regarded as the most correct since it does not rely on a track length estimator and gives an output of energy deposition as the energy balance in the tally cell, adjusted for relativistic changes in mass. Since ideally we want to test our method using two tally types a second best tally type had to be found. Also, if the two tally types are mixed, they had to be consistent, and work well in the mathematical method together.

Relative uncertainty was given in each of the MCNP runs. A relative uncertainty of 5% or less was deemed to be acceptable and ultimately this was achieved. Relative uncertainty or statistical uncertainty refers to the error associated with the stochastic particle transport simulation. The output of the tally cells for the test prostate case was treated as values in a matrix as were all other cases. One row of the matrix (the row transverse to the origin of the seed) was taken and run through the mathematical method by using IDL. A mock positron dose was acquired and used in the mathematical method to do this preliminary check. The *f8 and the f6 tally types gave the best result. Therefore an f6 tally was used for calculating the point kernels for the positron emitter and therapeutic isotope, while an *f8 tally was used to calculate the therapeutic and positron dose. The output was put into matrix form. The prostate case output was a 3 by 3 matrix and the breast case output was a 31 by 13 matrix. Because it cannot be guaranteed that all cases will have a square matrix, a program called Maple was used to run the mathematical method and do the necessary matrix operations. IDL cannot compute generalized inverses. The matrices were converted into Fourier space, and then the matrix inverse of the positron point kernel (G_p) was done. Because the matrices in breast case were not

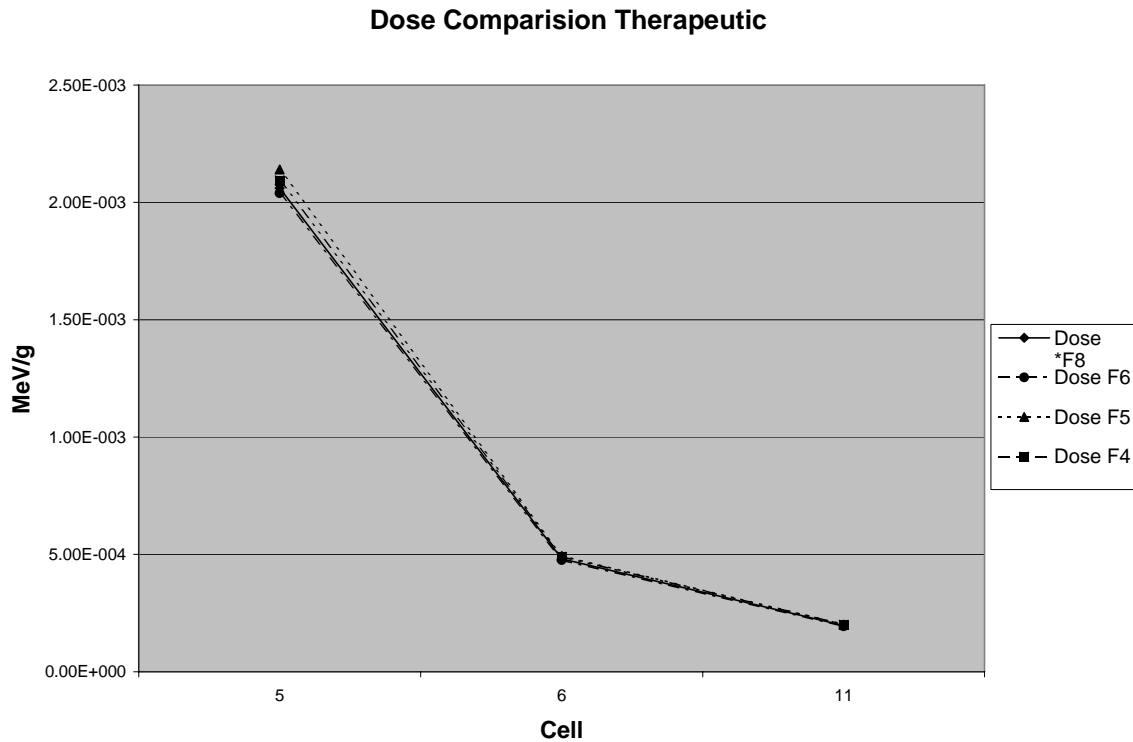


Figure 11-Dose Comparison of Tally Types

square, a generalized or Moore-Penrose inverse had to be found. Matrix multiplication was done, multiplying the inverse of the positron point kernel $[G_p]^{-1}$ with the therapeutic point kernel (G_t) and with the positron dose (D_p), as explained earlier in this chapter. This gave the therapeutic dose in Fourier space based on the mathematical method. An inverse Fourier transform was applied to put the therapeutic dose into real space. Since the final therapeutic dose is given in units of MeV it must be divided by the mass of the detector and converted into cGy to be compared to the Pinnacle output.

4.1.3 Data Analysis

The data analysis was primarily done in Microsoft Excel. Microsoft Excel has functions that were helpful and it was useful for converting the IDL output into spreadsheet form. Finding the Gaussian, fwhm, and the sigma values for the PET data was also done by using Excel. After Fourier transforming and inverse Fourier

transforming the imaginary part of the matrix values of the therapeutic dose were eliminated (because their magnitude was much less than the real part) and they were compared to the expected values by using Excel. The percent difference was found by subtracting the experimental value by the expected value, dividing the result by the expected value, and multiplying by one-hundred. Also, they were compared to values acquired by Pinnacle. Since Pinnacle does not have a seed comparable to the breast case, MCNP was used to obtain the radial dose functions. An f6 tally with ring detectors was used to get the dose. The centers of the detectors were spaced 1 mm apart starting 1.5 mm from the source and ending 4.15 cm from the source. The radial dose function accounts for the effects of absorption and scatter in the medium along the transverse axis of the source. The radial dose function applies only to the transverse axis and only to points with an angle equal to $\pi/2$ with respect to the longitudinal axis of the seed. The radial dose function defines the fall off in dose rate along the transverse axis due to absorption and scatter in the medium, but can also be influenced by filtration of photons by encapsulation and source materials. The radial dose function is normalized to the dose at one centimeter from the source and it is corrected by an r^2 factor where r is the distance from the source. A plotting software, Surfer, was used to construct the isodose curves to visually illustrate the comparison. Also, during one of the preliminary studies the mock infinite medium data was visually compared to the half sphere data by using Surfer to plot the isodose lines. It was quantitatively compared by using Microsoft Excel to get the percent difference, which will be presented in section 5.2.

CHAPTER 5

RESULTS

5.1 Seed in Prostate

As mentioned before, nine tally cells in a 3 by 3 matrix were used for this case. In the MC computations, the tally cells were constructed as ring detectors and tallied using f6 and *f8. The output for the nine tally cells using the SW mathematical method and by using MCNP was compared. As discussed earlier, several methods of redistributing the PET intensity values were explored. These methods were mainly explored in the Ir-192 case and will be discussed in the next section. Since the different methods do not result in a better agreement, the default (100 percent of the PET counts from the region within $\pm 3 \cdot \sigma$ was put into the seed region) was used for the prostate case. The detectors in the midplane of the seed had a discrepancy of 12 to 15 percent. The other detectors, off midplane, had discrepancy as high as 60 percent that decreased to as low as 20 percent as the distance from the seed increased.

Since the Pinnacle software only accepts activity in units of U, which is a measure of air kerma strength, $\text{cGy cm}^2 \text{hr}^{-1}$, a conversion to activity units are needed when the TG-43 method is used. TG-43 gives the activity of Pd-103 in both Curie and U units. An air kerma strength of 2.6 U is equivalent to an apparent activity of 2 mCi. The comparison of the MCNP output to the pinnacle results required this type of unit conversion. The f8 tally gives output in units of MeV per tally cell and is normalized to one photon. The mass of the detectors (or tally cell) is given in grams. In some cases where the geometry is complicated, MCNP is unable to accurately determine the mass of a detector. So mass was verified by determining it manually. The detector geometry was

a rectangular torus whose volume is $2*\pi*R*s^2$ (s is the side of the square and R is the radius of the midpoint of the torus). The density of the detector was water equivalent, so the volume in cm^3 was equivalent the mass in grams. To simplify the calculation process one hour implant duration was calculated by Pinnacle. The conversion from MCNP output to cGy for one hour of exposure time to a radio-isotope is as follows:

$$Dose\ rate\left[\frac{cGy}{hour}\right]=\frac{number\ of\ photons}{decay}\times\frac{number\ of\ decays}{second}\times\frac{3600\ sec}{hr}\times\frac{1}{mass\ in\ grams}$$

$$\times\frac{1000\ grams}{kilogram}\times 1.602176E-13\ \frac{J}{MeV}\times\frac{1\ Gy}{\frac{J}{kg}}\times\frac{100\ cGy}{Gy}\times MCNP\ output\left(\frac{MeV}{photon}\right).$$

$$Dose\ rate\left[\frac{cGy}{hour}\right]=5.7678E-5\times\frac{\frac{photon\ yield}{decay}\ Activity(Bq)}{mass\ of\ tally\ volume\ (g)}\times MCNP(F8\ tally)\left[\frac{MeV}{photon}\right]$$

The top three cells in the 3 by 3 matrix were the cells around the transverse center of the seed. The center of these detector cells were set to 0.2, 0.4, and 0.6 respectively. The dose for the mathematical method, the true or benchmark dose using MCNP, and the dose using pinnacle software were compared at these distances.

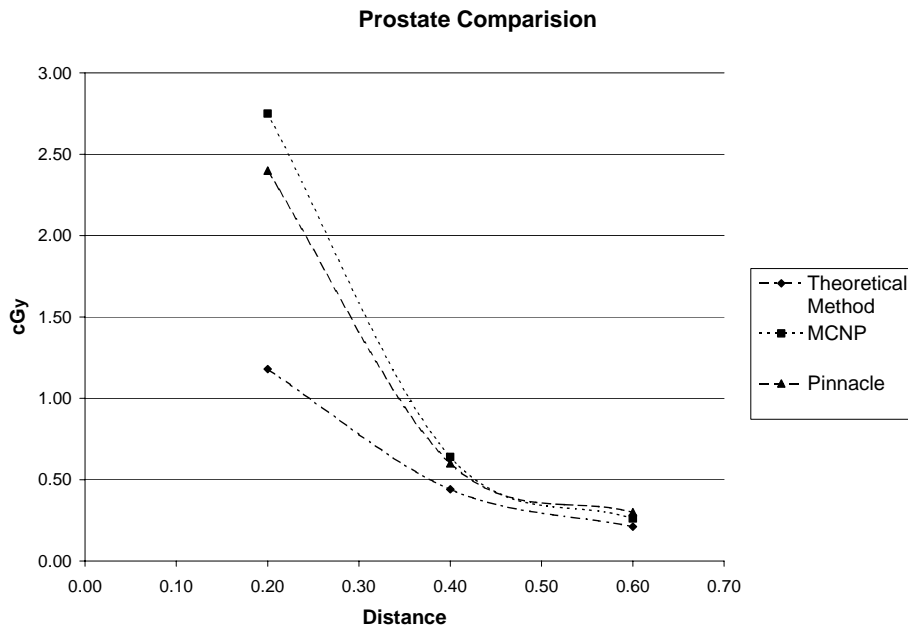


Figure 12 – Dose Comparison for the Prostate Case

The comparison showed that the SW method appreciably underestimates the dose close to the source, but converges to the benchmark dose farther from the source. The Pinnacle software seems to slightly underestimate dose close to the source and also converges on the benchmark dose as the distance from the source increases (this however can be the result of the small difference between the dimensions of the Pinnacle and the experimental Pd-103 seed). The ratio of doses was not constant as function of distance from the source (Fig. 13), therefore the difference in dose cannot be resolved by use of a simple multiplier. This is thought to be due to the blurring in the PET image. Computations using two theoretical PET images (a single idealized voxel source and a voxel core with simulated blurring, described later in this section) showed that the effect of blurring has an important contribution to the discrepancy. The method to partition the true counts and the false counts, thus, needs to be improved.

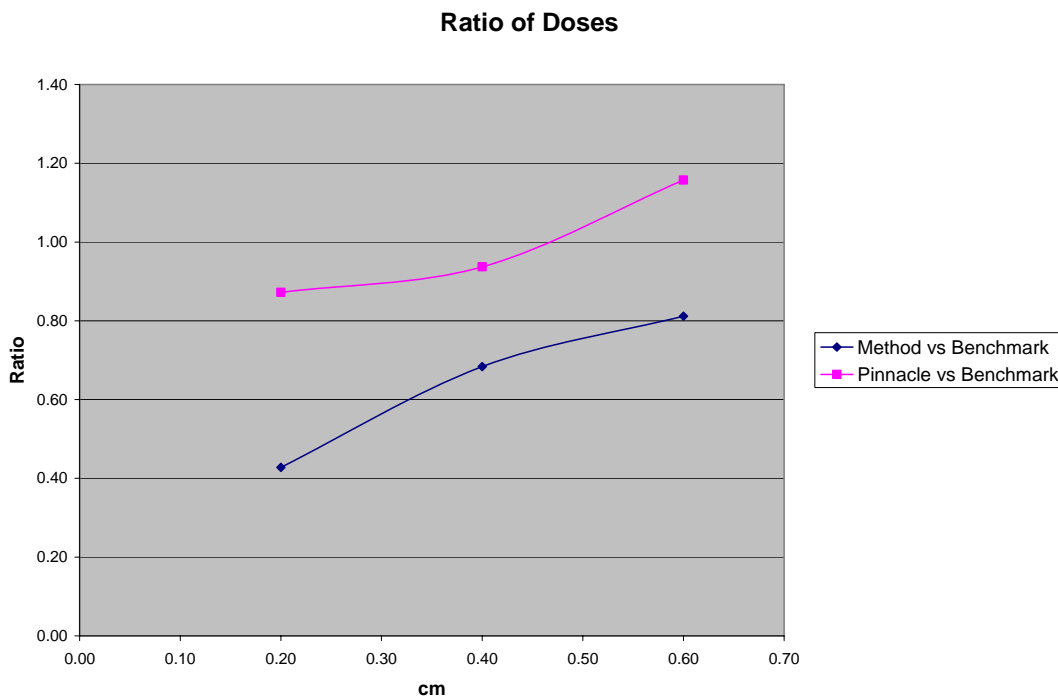


Figure 13-Ratio of Doses versus Benchmark Computation for Prostate Case

5.2 PET Intensity Redistribution to Improve Results

As mentioned earlier, several methods were explored to redistribute the PET intensity values. For the purpose of practicality using *apriori* knowledge and to get a lower discrepancy, the actual region of the seed was used to concentrate the counts.

In one method of redistributing the PET pixel intensity values, an assumption was made that a certain percentage of the values outside of the seed region are false and the complementary percentage of them are true. In general, the intensity redistribution process works by taking a portion of the values that go out to $3 \cdot \sigma$, summing them and multiplying the summed value by the percent that are assumed to be true counts, and adding them to the portion of the real seed to which they correspond. This process is done in the x, y, and z directions. Because the dimensions of the seed are known, and the peak centroid of the Gaussian is extracted from the image, the seed region could be determined. This is the region where the counts were added. The percentages that were evaluated as true intensity were 25, 50, 75, and 100. The difference in the resulting dose (normalized to one source photon) for these percentages was very slight. The discrepancy for the 25 and 75 percent were slightly higher than the 100 percent. The discrepancy for 50 percent was nearly identical to the discrepancy for 100 percent.

Another method of redistributing the PET pixel intensity values was to square the pixel intensity value and divide it by the sum of intensities in all pixels. This was a variable redistribution method unlike the others that just involved multiplying by a constant. The discrepancy from this method was somewhat higher, but resulted in a more continuous decrease in discrepancy over distance (Fig. 16). It is evident that the pixel intensity redistribution method is an important factor in reducing the discrepancies. No

other methods were investigated in this research, but it is recommended that future efforts be made in this area.

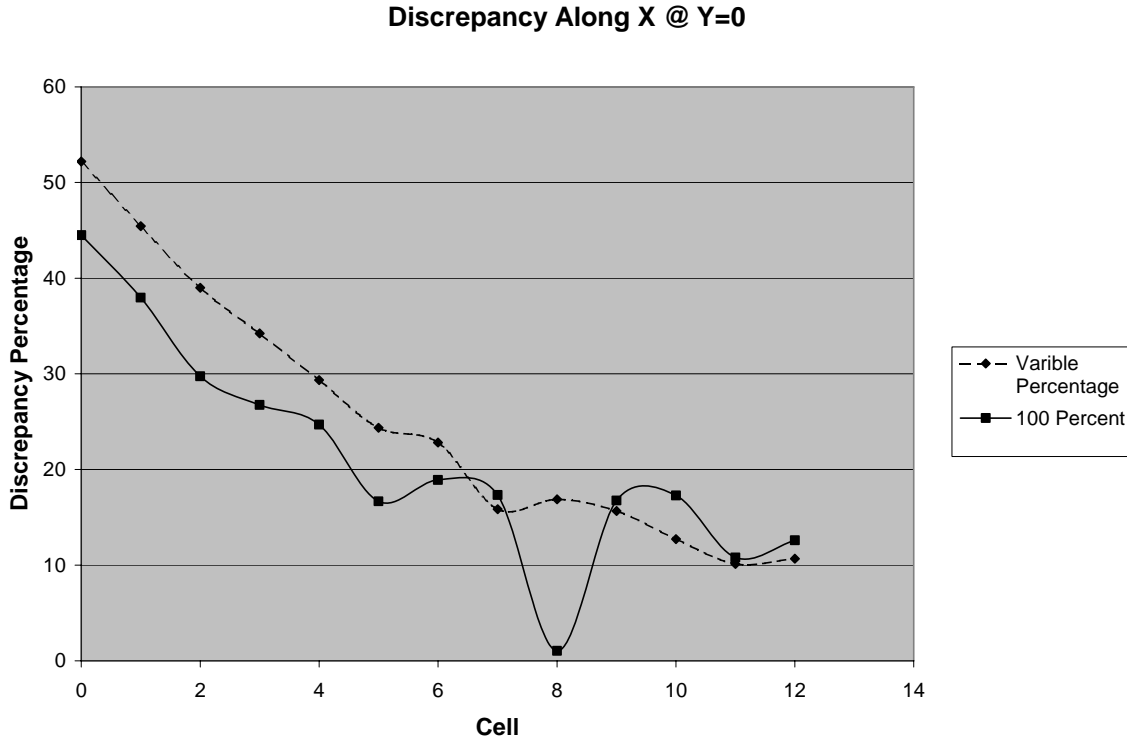


Figure 14-Discrepancy Comparison of Variable Percentage vs. 100 Percent in the Breast Case.

5.3 Seed in Breast

Unlike the prostate seed study this was a 31 by 13 matrix, and instead of being ring detectors it was a collection of rectangular detectors the same size as the voxels registered in the PET/CT. The full sphere versus half sphere comparison in the preliminary study resulted in a difference of greater than 10%.

Over the course of the project it was found that the assumption that all positrons were annihilated only in the seed wall was not necessarily true. Ultimately, both the seed wall and the internal part of the seed were regarded as the source of the 511 keV

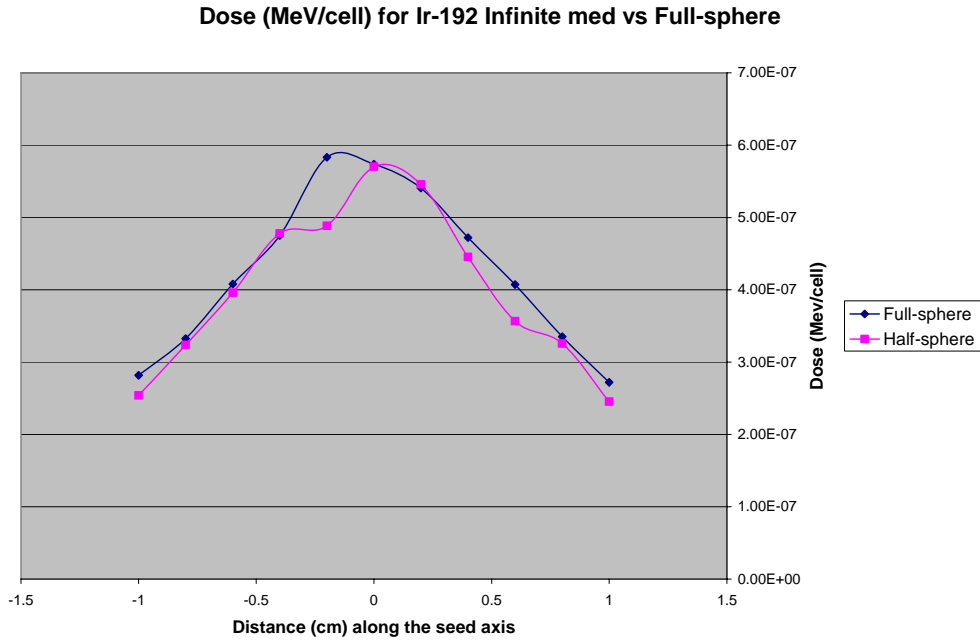


Figure 15-Half-sphere (finite medium) vs. Full-sphere (infinite medium) Dose Comparison at 4 mm from the Transverse Axis of the Seed

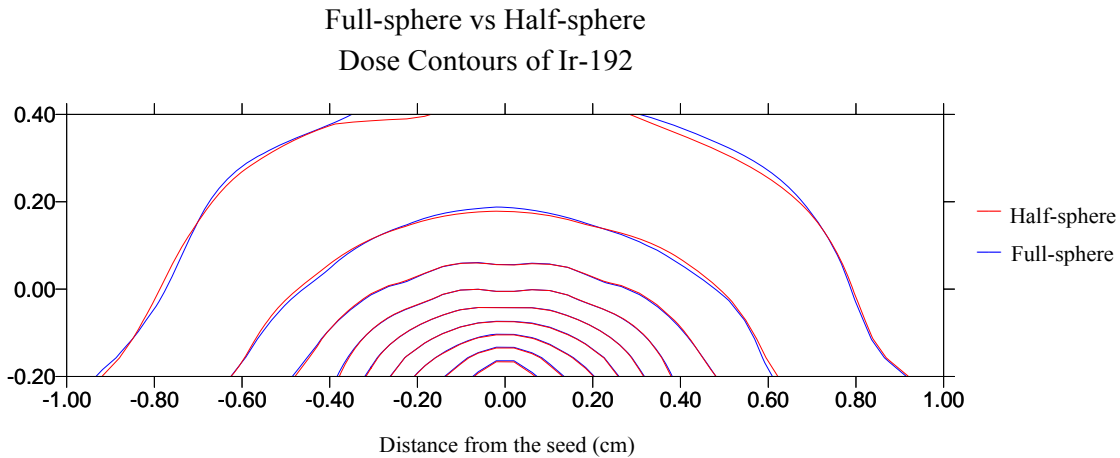


Figure 16-Half-sphere vs. Full-sphere Dose Contours

annihilation photons. Prior to regarding both of these as source, the discrepancy very close to the source was as high as 600%. After regarding both as source the discrepancy in the worst performing voxel decreased to 44%. The majority of the cells had a

discrepancy of less than 20 percent, and as in the prostate case, it decreases as the distance from the source increases.

For the purpose of calculated dose comparisons in the breast phantom, air kerma strengths in terms of $\text{cGy cm}^2 \text{hr}^{-1}$ (commonly referred to as U) were acquired for Ir-192 to obtain the Pinnacle results. TG-43 states that for Ir-192 air kerma strength of 29000-41000 U is equivalent to 7-10 Ci. To ensure accuracy, the mass of the MC detectors was verified by manual computations where MCNP indicated difficulties. The volume of the detectors was equal to $s^2 \cdot \text{depth}$ (once again s is the length of a side). Also, we obtained the radial dose function for the Ir-192 seed to be used in Pinnacle. This was done by doing an MCNP run and multiplying the output by distance squared and dividing by the output at 1 cm out from the source. The method of getting radial dose was verified by checking it with an existing seed with a known radial dose function.

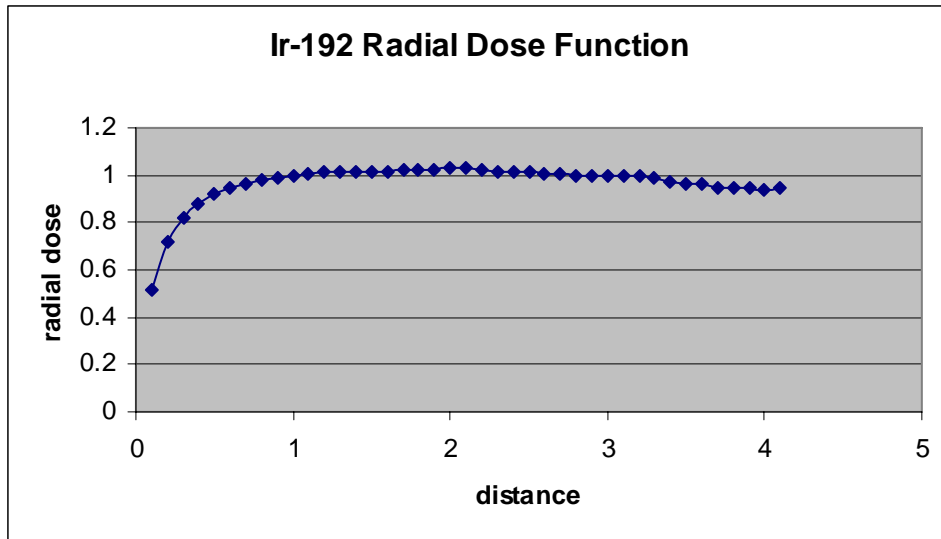


Figure 17-Calculated Radial Dose Function for Ir-192

The dose comparison for the breast case showed that the therapeutic dose using the Sajo-Williams (SW) method is very close to the Pinnacle dose, but both are

significantly lower than the MCNP benchmark dose close to the source. It is a possibility that for higher energy isotopes Pinnacle underestimates dose close to the source. The underprediction of the Sajo-Williams method, however, may be due to PET blurring artifacts close to the source. Nevertheless, the three dose types converge around 4 mm just as it did in the prostate case.

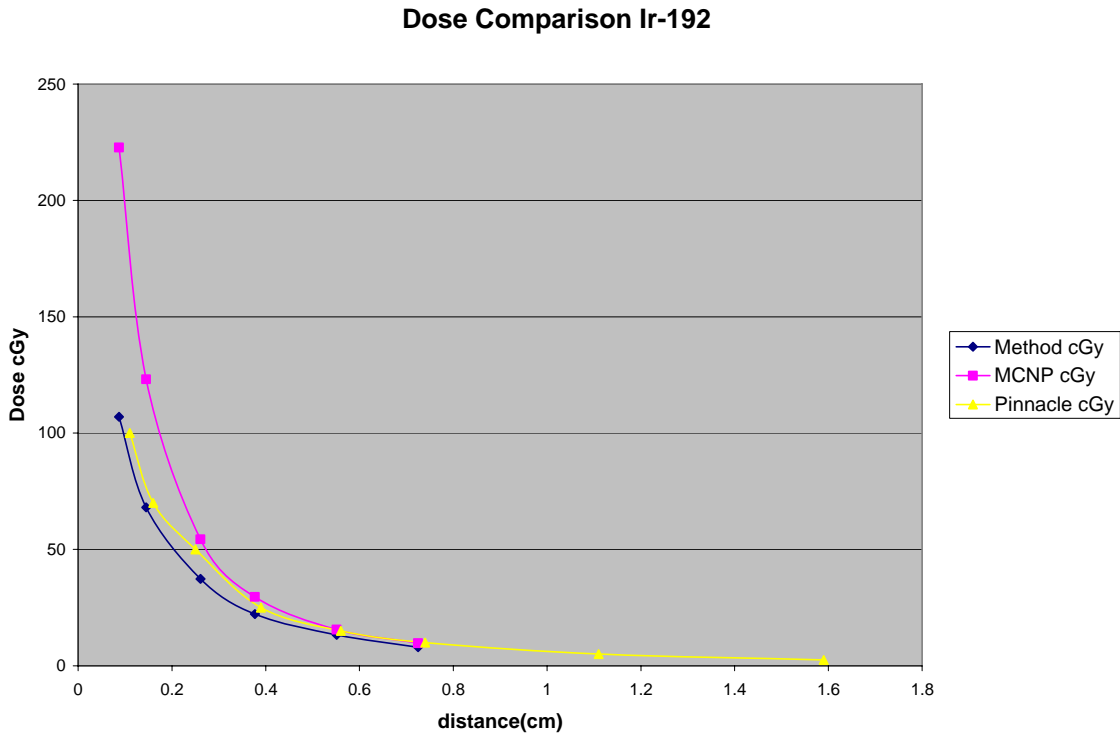


Figure 18-Dose Comparison for the Breast Case

5.4 Analysis of Results

Initially, it was thought that use of the f6 tally was responsible for the discrepancy close to the source. This is because f6 is a kerma tally, which is known to overpredict the dose in regions of electronic disequilibrium that may occur close to the source. This possibility was explored and it was found that the difference between the f6 and the *f8 tally was nearly negligible at distances of dosimetric interest. Nevertheless the Sajo-

Williams method was re-done for the prostate case using solely *f8 tallies and the resulting data showed that there was no significant difference from the original method (Fig. 19).

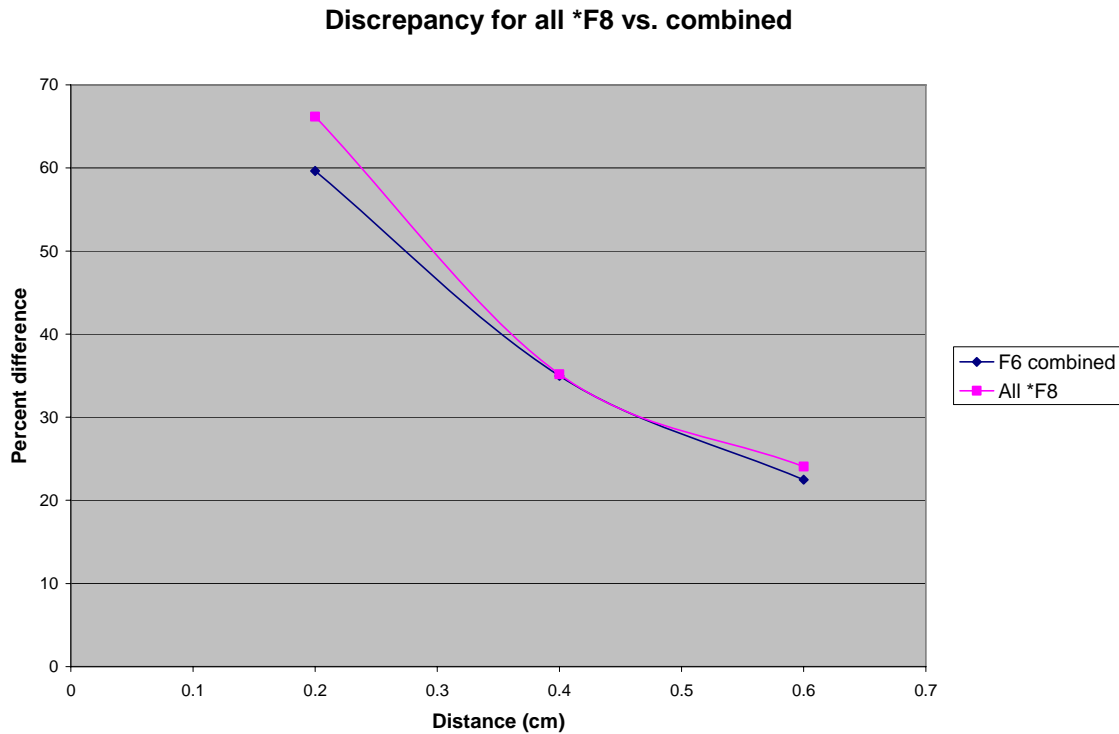


Figure 19-Discrepancy Comparison for Using only *f8 Tallies vs. Combined *f8 and f6

The effect of PET blurring:

Based on the results of the dose comparison for the prostate case the effect of blurring on the SW method was brought into question. A computational exercise was done to explore the effect of blurring on the accuracy of dose. It was found that blurring has a significant effect on the dose when computed using MC or by the SW method. For a standard seed an idealized hypothetical PET trial was compared to a hypothetical blurred PET trial and they were put through the Sajo-Williams method. Figure 20a shows the computational geometry: an idealized single voxel source of 511 keV photons is

placed in the center, and surrounded by tally voxels whose size and distribution are identical to the actual PET image voxels. Figure 20b is the same geometry, but it has a somewhat realistic blurring introduced \pm one voxel from the center voxel in all directions, surrounding the core (only 2D is shown here). The simulated PET intensity falls off as a factor of 0.6 of the nearest neighbor. This is a symmetric blurring.

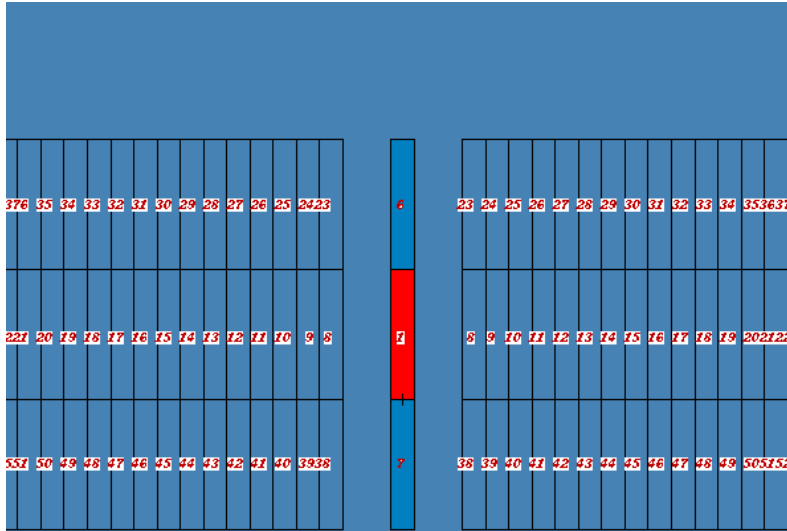


Figure 20a-Idealized Geometry with a Single Voxel Source

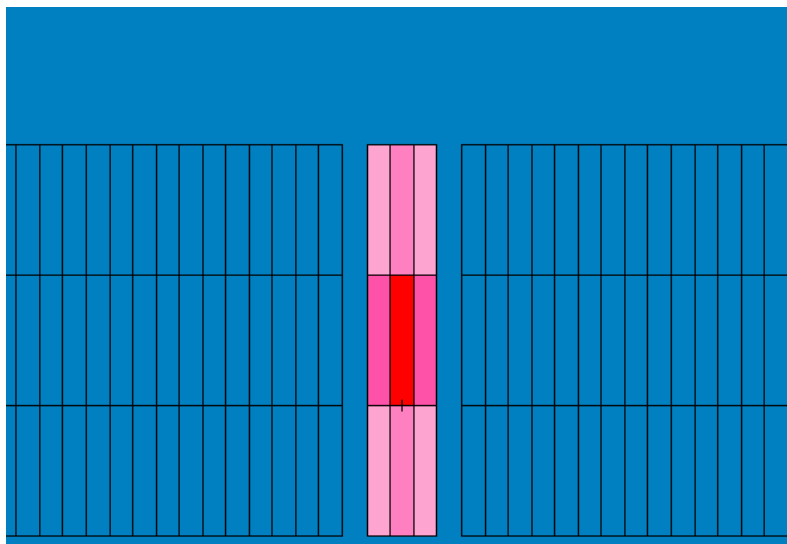


Figure 20b-Idealized Geometry with Blurred Source

As shown in Figure 21, on the midplane of the seed blurring results in an under-prediction of the dose close to the seed, by about 25%. However, off the midplane, blurring will result in an overprediction of the dose by about also 25%. This is because of two reasons; (a) the PET source is voxelized, that is the source is rectangular. If the tally cells are circular, there will be places where the corners of the voxels are close to the tally cell in the vicinity of the source. (b) More importantly, the discrepancy varies a great deal with the type of blurring introduced. Here the blurring is introduced about the center voxel within one voxel distance in all directions. Thus, this +/- 25% discrepancy at the source is a limiting condition for this kind of blurring. Hence, in practice, a method must be found that not only recaptures the PET counts but puts them in the least number of voxels.

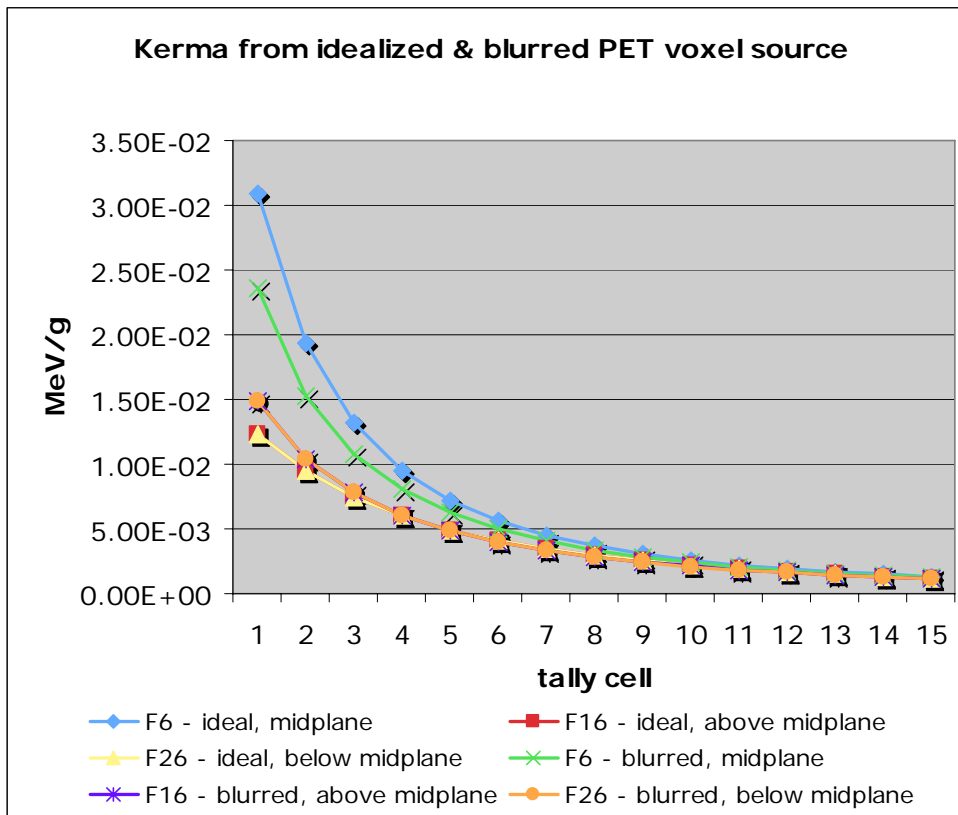


Figure 21-Kerma Comparison of Ideal vs. Blurred

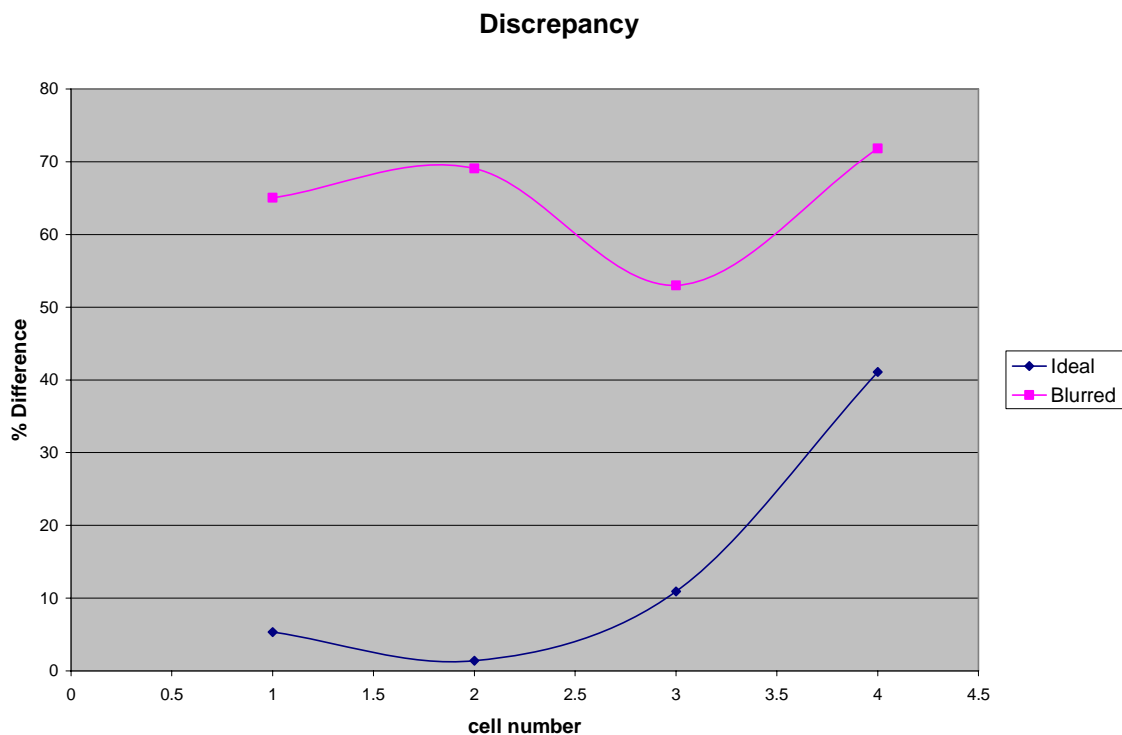


Figure 22. Discrepancy in Dose Using Ideal vs Blurred PET Image

After applying the Sajo-Williams dose reconstruction method, the discrepancy for the ideal and the blurred case was even greater. Figure 22 shows the difference between the SW and the MC dose computations. The increasing discrepancy for the ideal case with increasing distance from the source does not appear to be correct, and it does not confirm our earlier findings. It is possibly due to a yet unidentified numerical error in the computations. Also, it is important to realize that when the generalized matrix inversion is used, the order of matrix multiplication in Eq(3) depends on the rank of the inverse matrix. For the case of the ideal vs. blurred comparison the rank was equivalent to the number of columns.

CHAPTER 6

SUMMARY

A new technique using direct post-implant dosimetry, which does not depend explicitly on seed orientation or position, was explored. Dose point kernels were obtained using Monte Carlo simulation for a single seed breast and prostate geometry. Green's functions were found for the positron marker and therapeutic photons. Various dose computation options in MCNP were compared and the tally types of *f8 and f6 (dose and kerma, respectively) were determined to be the best pair. A single seed was imaged for a prostate phantom and a breast phantom using a PET/CT. The pixel-wise image intensity data were extracted and used to obtain dose using MC computations for the annihilation photons for the experimental seeds. The Sajo-Williams dose reconstruction method was used to compute the therapeutic dose of the seed based on the positron marker dose. The therapeutic dose was also computed using the Pinnacle planning software. A benchmark Monte Carlo model was done to compute the therapeutic and positron doses where the precise seed geometry with source energies and distributions were known. The therapeutic dose computed using Pinnacle, computed using the Sajo-Williams method, and computed in the benchmark run was compared.

It was found that the Sajo-Williams method generally underpredicts the dose close to the source. The two main issues based on the results appear to be the discrepancy close to the source (within 4 mm) and the effect of blurring on the PET image. However, they are not independent: In a control case it was found that blurring can indeed affect dose significantly. In a series of test cases, we proved that the cause of the discrepancy in dose that is found close to the source is blurring. Although several attempts were made to

resolve this issue, one has not been found that completely solves it. However, in practice the dose very close to the source is not as important as farther away. The method of obtaining therapeutic dose investigated in this thesis can yield good results when far enough out from the source. The distance where the discrepancy from the benchmark case is reduced to within 5% is about 0.5 cm for the breast implant case and approximately 1 cm for the prostate case. A better source redefinition method than those used in this thesis is expected to further reduce the discrepancies.

Conclusions:

1. Breast case
 - 1a. The Sajo-Williams method has a good agreement with Pinnacle dose computations.
 - 1b. Both Pinnacle and the Sajo-Williams method under-predicted the dose with respect to the MC benchmark.
2. Prostate case
 - 2a. Pinnacle somewhat under-predicted the dose in the MCNP benchmark.
 - 2b. The Sajo-Williams method appreciably under-predicted the dose compared to the benchmark.
3. Possible reasons for under-prediction:
 - 3a. In the prostate case there were too few matrix elements, only a 3x3 dose matrix was considered, whereas the breast case, where the agreement is much better, a 21x13 dose matrix was used. This points to the possibility of numerical instability.

- 3b. In all cases PET image blurring imposes a limiting condition on the accuracy of the Sajo-Williams method, as shown in section 5.4.
- 3c. Current PET image reconstruction protocols are optimized for positron activity in the body in normal form (injected as a liquid solution). This way, the positron range is determined by the stopping power of the tissue, and significant blurring occurs. The PET image reconstruction algorithm is optimized with the presence of blurring: That is, the blurring effect is built in the reconstruction algorithm (a.k.a. kernel). Thus, it cannot take advantage of limited range blurring by a high-Z object, such as the seed wall, and possibly gives even worse results when no range blurring is present. Thus, to reduce the range blurring effects, the kernel of the reconstruction should be modified.
- 3d. The manufacturer regards the details about the kernel as proprietary information. In lack of access to the kernel, other methods for PET image intensity redistribution should be investigated. Deblurring methods, used in commercial photography industry, may be a viable alternative.
4. The good agreement with Pinnacle results in the breast case shows the potential of the Sajo-Williams method. If the computational algorithm presented in this thesis and in [1] is fully developed, it could give the dose distribution as soon as the PET image acquisition is completed. Whereas using Pinnacle or other seed dosimetry software entails much of the time of the physicist and is subject of non-trivial subjective and objective errors.

REFERENCES

- Berger, MJ. ESTAR, PSTAR, and ASTAR: Computer Programs for Calculating Stopping-Power and Range Tables for Electrons, Protons, and Helium Ions. Report NISTIR 4999, National Institute of Standards and Technology, Gaithersburg, MD, 1993.
- Bice WS, Dubois DF, Prete JJ, Prestidge BR. Source localization from axial image sets by iterative relaxation of the nearest neighbor criterion. *Medical Physics* 26(9):1919-1924; 1999.
- Briesmeister JF, ed. MCNP - A general Monte Carlo N-particle transport code. Version 5. LA 12625, Los Alamos National Laboratory, 2003.
- Brinkmann DH, Kline RW. Automated seed localization from CT datasets of the prostate. *Medical Physics* 25(9):1667-1672;
- Carrier JF, Beaulieu L, Therriault-Proulx F, Roy R (2006). "Impact of interseed attenuation and tissue composition for permanent prostate implants." *Medical Physics* 33 (3) 595 – 604.
- DeMarco JJ, Hugo G, Solberg TD. Dosimetric parameters for three low-energy brachytherapy sources using the Monte Carlo N-Particle code. *Medical Physics* 29(5); 662-668; 2002.
- Hendee WR, Ibbott GS. *Radiation Therapy Physics*. Mosby 1999.
- ICRU Report 37: Stopping Powers for Electrons and Positrons. International Commission on Radiation Units and Measurements, 1984.
- Khan FM, *The Physics of Radiation Therapy*. Lippincott Williams & Wilkins, 2003.
- Jarrett JM, Sajo E. Experimental Method Development for Direct Dosimetry of Permanent Prostate Brachytherapy Implants. Abstract, *Medical Physics* v 32 n 6, p. 1950, 2005.
- Jones WF, Casey ME, van Lingen A, Bendriem B. LSO PET/SPECT Spatial Resolution: Critical On-line DOI Rebinning Methods and Results. Nuclear Science Symposium and Medical Imaging Conference Lyon, France October 15-20, 2000.
- Johnson and Johnson Corporation. Theraseed. Pd-103, a minimally invasive option for prostate cancer. Information for physicians, 1998.
- Kocher DC. Radioactive decay data tables. DOE/TIC-11026, Technical Information Center, U.S. Department of Energy, Washington, D.C., 1981.

- Li Z, Fan JJ, Palta JR. Experimental measurements of dosimetric parameters on the transverse axis of a new ^{125}I source. *Medical Physics* 27 (6); 1275-1280; 2000.
- Moerland MA, Wijrdeman HK, Beersma R, Bakker CJG, Battermann JJ. Evaluation of permanent I-125 prostate implants using radiography and magnetic resonance imaging. *Int. J. Radiat. Oncol., Biol. Phys.* 7, 927-933;1997.
- Nath R, Anderson LL, Luxton G, Weaver KA, Williamson JF, Meigooni AS. Dosimetry of interstitial brachytherapy sources: Recommendations of the AAPM Radiation Therapy Committee Task Group No. 43. *Medical Physics* 22(2); 209-234; 1995.
- North American Scientific. MED3633 Pd-103 brachytherapy source. Information for physicians. April 1999.
- Prestidge BR, Bice WS, Kiefer EJ, Prete JJ. Timing of computed tomography-based postimplant assessment following permanent transperineal prostate brachytherapy. *Int J Radiat Oncol Biol Phys* 43(5):1169-70; 1999.
- Rivard MJ, Coursey BM, DeWerd LA, Hanson WF, Huq MS, Ibbott GS, Mitch MG, Nath R, Williamson JF. Update of AAPM Task Group No. 43 Report: A revised AAPM protocol for brachytherapy dose calculations. *Medical Physics* 31(3) 633-674, 2004.
- Roberson PL, Narayana V, McShan DL, Winfield RJ, McLaughlin PW. Source placement error for permanent implant of the prostate. *Medical Physics* 24(2):251-257; 1997.
- Roy JN, Wallner KE, Harrington PJ, Ling CC, Anderson LL. A CT-based evaluation method for permanent implants: application to prostate. *Int J Radiat Oncol Biol Phys* 30;26(1):163-9; 1993.
- Sajo E, Williams ML. Embedded Radiation Emitter for the Localization and Dosimetry of Brachytherapy Seed Implants. US Patent 6,761,679; 2004.
- Sajo E, Williams ML. Post-Implant Prostate Dosimetry without Seed Localization. *Medical Physics* 31(6) p. 1747, 2004.
- Shultis JK, Faw RE. *Radiation Shielding*. American Nuclear Society, 2000.
- Tubic D, Zaccarin A, Pouliot J, Beaulieu L. Automated seed detection and 3D reconstruction I: Seed Localization from Fluoroscopic Images or Radiographs. *Med Phys* 28(11):2265-2271; 2001.
- Willins J, Wallner K. CT-based dosimetry for transperineal I-125 prostate brachytherapy. *Int J Radiat Oncol Biol Phys* 1;39(2):347-53; 1997.

Yegin G, D Rogers. "A Fast Monte Carlo code for Multi-seed Brachytherapy Treatments, Including Inter-Seed Effects." Abstracts, Medical Physics 31 (6) p. 1771, 2004.

APPENDIX A

SAMPLE MCNP INPUT FILE

Pd-103dose in water from one nearest seed. Pd thickness is 23 um

```

c
c 1      5  -1.0    -3 4 -6
c              inner seed cell
c
c 2      3  -7.96   -1 2 -5 #(-3 4 -6)
c              outer seed cell
c
c 3      5  -1.0    -7 #5 #6 #7 #8 #9 #10 #11 #12 #13
c              #(23 -27 28 -21 18 -20)
c              tissue
c
c 4      0          7
c              universe outside
c
c 5      5  -1.0    10 -11 -8 9
c
c 6      5  -1.0    13 -14 -8 9
c
c 7      5  -1.0    10 -11 -12 8
c
c 8      5  -1.0    13 -14 -12 8
c
c 9      5  -1.0    10 -11 -15 12
c
c 10     5  -1.0    13 -14 -15 12
c
c 11     5  -1.0    16 -17 -8 9
c
c 12     5  -1.0    16 -17 -12 8
c
c 13     5  -1.0    16 -17 -15 12
c
c 14     5  -1.0    -24 23 -21 22 -25 18
c
c 15     LIKE 14 BUT trcl (0.0585 0.0000 0)
c
c 16     LIKE 14 BUT trcl (0.0000 -0.0585 0)
c
c 17     LIKE 14 BUT trcl (0.0585 -0.0585 0)
c
c 18     5  -1.0    -24 23 -21 22 -26 25
c
c 19     LIKE 18 BUT trcl (0.0585 0.0000 0)
c
c 20     LIKE 18 BUT trcl (0.0000 -0.0585 0)
c
c 21     LIKE 18 BUT trcl (0.0585 -0.0585 0)
c
c 22     5  -1.0    -24 23 -21 22 -20 26
c
c 23     LIKE 22 BUT trcl (0.0585 0.0000 0)
c
c 24     LIKE 22 BUT trcl (0.0000 -0.0585 0)
c
c 25     LIKE 22 BUT trcl (0.0585 -0.0585 0)
c
c

```

```

c
c          ***** end of cell definitions *****
c =====
c
c          ***** Bounding surfaces *****

1      pz   0.26          $top of seed
2      pz  -0.26          $base of seed
3      pz   0.25          $top of inner
4      pz  -0.25          $base of inner
5      cz   0.04          $radius outer
6      cz   0.03          $radius inner
7      so   1.5           $radius of universe
8      pz   0.05
9      pz  -0.05
10     cz   0.15
11     cz   0.25
12     pz   0.15
13     cz   0.35
14     cz   0.45
15     pz   0.25
16     cz   0.55
17     cz   0.65
18     pz  -0.4905
19     pz   0.0
20     pz   0.4905
21     py   0.0585
22     py   0.0
23     px  -0.0585
24     px   0.0
25     pz  -0.1635
26     pz   0.1635
27     px   0.0585
28     py  -0.0585
c
c
c          ***** end definitions of bounding surfaces *****
c =====
c
c          ***** set other calculation parameters *****

mode    p e
c
c Importances: play Russian roulette in detectors
imp:p    4 0 4 20R
imp:e    4 0 4 20R
c =====
c
c          ***** source definition *****
c 0.511 source.
c   Source is in encapsulation
c
c sdef  erg=0.511 par=2 cel=d1 axs=1 0 0
c
c   sil L 14
c         15
c         16
c         17
c         18
c         19
c         20
c         21
c         22

```

```

23
24
25
spl V 2810173.8
      2702376.9
      2203022.1
      2746429.1
      3178383.5
      2887297.1
      2327467
      2874353
      2436068.5
      2263095.3
      1853865.3
      2171014.5
c
c Note that MCNP will calculate detector response normalized to 1 source
c photon regardless to yield
c =====
c
c          ***** define desired tallies *****
c
c *f8:p,e 5 6 7 8 9 10 11 12 13
c
c =====
c
c          **** define materials in problem ****
c 1: Pb
c 2: C
c 3: Stainless steel
c 4: Air (from NIST)
c 5: H2O, weight fraction from NIST) ESTEP = 8 is not needed now
c 6: Pd
c m1 82000 -1
c m2 6000 -1
m3 14000 -0.01 24000 -0.17 25000 -0.02 26000 -0.655 28000 -0.12 42000 -0.025
c m4 6000 -1.24E-4 7000 -0.7552676 8000 -0.231781 18000 -0.012827
m5 1000 -0.111894 8000 -0.888106 estep=8
c m6 46000 -1
c =====
c          ***** Energy and cutoff cards *****
c phys:e 0.511
c cut:e 1.0E8 0.0005
c =====
c void
nps 4e2
prtmp 3j 1 $ retain only the last 1 dump in the mctal (bin) file
print 110 128

end of input

```

APPENDIX B

IDL DATA EXTRACTION PROGRAM FOR DICOM

```
pro printelement3, filename

img2=fltarr(3080192)
l=01
values=fltarr(47)

for i=1,47 do begin
filename=strcompress(i,/remove_all)
img=read_dicom(filename)
;tvsc1, img
;img2=float(img)
obj=OBJ_NEW('IDLffDICOM')
read=obj->Read(filename)
value=obj->GetValue('0028'x,'1053'x)
;print, *value[0]
;img3=*img[0]* *value[0]
values[i-1]=*value[0]

for j=01,65535 do begin
img2[l]=img[j]
l=l+1
endfor
;img2=*img2[0]*values[i-1]
;plot, img2
;print, img2
endfor
print, values
;max3=max(img2,cor)
;print, cor
max1=max(values,b)
print, b
file1=strcompress(b, /remove_all)
f1=read_dicom(file1)
max2=max(f1,p)
print, p
print, max2*values[b]
s=p mod 256
t=(p-s)/256
img2=reform(img2,256,256,47)
;print, s, t
print, img2[s,t,b]
;openu,1,'out1.txt',append
;printf,1,f1
img4=fltarr(15,15,15)
for z=0,14 do begin
file2=strcompress((b-7+z),/remove_all)
f2=fltarr(256,256)
```

```

f2=read_dicom(file2)
;f2=bytscal(f2)

for v=0,14 do begin
img4[0,v,z]=f2[s-7,t-7+v]*values[16+z]
img4[1,v,z]=f2[s-6,t-7+v]*values[16+z]
img4[2,v,z]=f2[s-5,t-7+v]*values[16+z]
img4[3,v,z]=f2[s-4,t-7+v]*values[16+z]
img4[4,v,z]=f2[s-3,t-7+v]*values[16+z]
img4[5,v,z]=f2[s-2,t-7+v]*values[16+z]
img4[6,v,z]=f2[s-1,t-7+v]*values[16+z]
img4[7,v,z]=f2[s-0,t-7+v]*values[16+z]
img4[8,v,z]=f2[s+1,t-7+v]*values[16+z]
img4[9,v,z]=f2[s+2,t-7+v]*values[16+z]
img4[10,v,z]=f2[s+3,t-7+v]*values[16+z]
img4[11,v,z]=f2[s+4,t-7+v]*values[16+z]
img4[12,v,z]=f2[s+5,t-7+v]*values[16+z]
img4[13,v,z]=f2[s+6,t-7+v]*values[16+z]
img4[14,v,z]=f2[s+7,t-7+v]*values[16+z]
endfor
endfor
;img4=bytscal(img4)
;print, img4
openu,3,'out2.txt',/append
printf,3,img4
print,img4[7,7,7]
;for w=0,46 do begin
file3=strcompress(b,/remove_all)
obj=OBJ_NEW('IDLffDICOM')
read=obj->read(file3)
obj->DumpElements, 'c:\rsi\elements.dmp'
;tv, f1
;print, *value3[0]
;value4=fltarr(47)
;value4[w]=value3[0]
;endfor
;openu,4,'out4.txt', /append
;printf,4,value3
;plot,f3
end

```

APPENDIX C

SAMPLE MAPLE PROGRAM FOR THE METHOD

with (Spread)

[*CopySelection, CreateSpreadsheet, EvaluateCurrentSelection, EvaluateSpreadsheet, GetCellFormula, GetCellValue, GetFormulaeMatrix, GetMaxCols, GetMaxRows, GetSelection, GetValuesMatrix, InsertMatrixIntoSelection, IsStale, SetCellFormula, SetMatrix, SetSelection*]

a																														
	A	B	C	D	E	F	G	H	I	J	K	L	M	N	O	P	Q	R	S	T	U	V	W	X	Y	Z	A	A	A	A
																											A	B	C	D
1																														
2																														
3																														
4																														
5																														
6																														
7																														
8																														
9																														
10																														
11																														
12																														
13																														
14																														
15																														
16																														
17																														
18																														
19																														
20																														
21																														

[&x, Add, Adjoint, BackwardSubstitute, BandMatrix, Basis, BezoutMatrix, BidiagonalForm, BilinearForm, CharacteristicMatrix, CharacteristicPolynomial, Column, ColumnDimension, ColumnOperation, ColumnSpace, CompanionMatrix, ConditionNumber, ConstantMatrix, ConstantVector, Copy, CreatePermutation, CrossProduct, DeleteColumn, DeleteRow, Determinant, Diagonal, DiagonalMatrix, Dimension, Dimensions, DotProduct, EigenConditionNumbers, Eigenvalues, Eigenvectors, Equal, ForwardSubstitute, FrobeniusForm, GaussianElimination, GenerateEquations, GenerateMatrix, GetResultDataType, GetResultShape, GivensRotationMatrix, GramSchmidt, HankelMatrix, HermiteForm, HermitianTranspose, HessenbergForm, HilbertMatrix, HouseholderMatrix, IdentityMatrix, IntersectionBasis, IsDefinite, IsOrthogonal, IsSimilar, IsUnitary, JordanBlockMatrix, JordanForm, LA_Main, LUdecomposition, LeastSquares, LinearSolve, Map, Map2, MatrixAdd, MatrixExponential, MatrixFunction, MatrixInverse, MatrixMatrixMultiply, MatrixNorm, MatrixPower, MatrixScalarMultiply, MatrixVectorMultiply, MinimalPolynomial, Minor, Modular, Multiply, NoUserValue, Norm, Normalize, NullSpace, OuterProductMatrix, Permanent, Pivot, PopovForm, QRdecomposition, RandomMatrix, RandomVector, Rank, RationalCanonicalForm, ReducedRowEchelonForm, Row, RowDimension, RowOperation, RowSpace, ScalarMatrix, ScalarMultiply, ScalarVector, SchurForm, SingularValues, SmithForm, SubMatrix, SubVector, SumBasis, SylvesterMatrix, ToeplitzMatrix, Trace, Transpose, TridiagonalForm, UnitVector, VandermondeMatrix, VectorAdd, VectorAngle, VectorMatrixMultiply, VectorNorm, VectorScalarMultiply, ZeroMatrix, ZeroVector, Zip]

>

>

b																															
	A	B	C	D	E	F	G	H	I	J	K	L	M	N	O	P	Q	R	S	T	U	V	W	X	Y	Z	A	A	A	A	
																												A	B	C	D
1																															

>

>

b2																														
	A	B	C	D	E	F	G	H	I	J	K	L	M	N	O	P	Q	R	S	T	U	V	W	X	Y	Z	A	A	A	A
																											A	A	A	A
	A	B	C	D																										
1																														
2																														
3																														
4																														
5																														
6																														
7																														
8																														
9																														
10																														
11																														
12																														
13																														
14																														
15																														
16																														
17																														
18																														
19																														
20																														
21																														
22																														
23																														
24																														
25																														
26																														
27																														
28																														
29																														
30																														
31																														
32																														

Dp:=GetValuesMatrix(b2)

Warning, inserted missing semicolon at end of statement

$$Dp := \begin{bmatrix} 0.000323 & 0.000197 & 0.000133 \\ 0.000295 & 0.000186 & 0.000131 \\ 0.000237 & 0.000164 & 0.000122 \end{bmatrix}$$

>

> *with(DiscreteTransforms)*

[FourierTransform, InverseFourierTransform]

> *gpf := FourierTransform(gp)*

$$gpf := \begin{bmatrix} [0.00065299999999999935 + 0. I, \\ 0.000163500000000000017 - 0.0000516728490924715204 I, \\ 0.000163500000000000017 + 0.0000516728490924715204 I], \\ [0.000061499999999999906 - 0.0000493634480157130104 I, \\ 0.000040499999999999952 - 0.0000360843918243516123 I, \\ 0.000048499999999999930 - 0.0000280014880556968480 I], \\ [0.000061499999999999906 + 0.0000493634480157130104 I, \\ 0.000048499999999999930 + 0.0000280014880556968480 I, \\ 0.000040499999999999952 + 0.0000360843918243516123 I] \end{bmatrix}$$

> *gtf := FourierTransform(gt)*

$$\begin{aligned}
gtf := & \left[\begin{aligned}
& [0.0000329566666666666690 + 0. I, \\
& 0.00000772166666666666756 - \\
& \quad 0.00000290118510267786884 I, \\
& 0.00000772166666666666756 \\
& \quad + 0.00000290118510267786884 I], [\\
& 0.00000602166666666666774 - \\
& \quad 0.00000413671467874366933 I, \\
& 0.00000365166666666666630 - \\
& \quad 0.00000306284317805096414 I, \\
& 0.00000467666666666666622 - \\
& \quad 0.00000189370888294197222 I], [\\
& 0.00000602166666666666774 \\
& \quad + 0.00000413671467874366933 I, \\
& 0.00000467666666666666622 \\
& \quad + 0.00000189370888294197222 I, \\
& 0.00000365166666666666630 \\
& \quad + 0.00000306284317805096414 I]
\end{aligned} \right]
\end{aligned}$$

> $Dpf := \text{FourierTransform}(Dp)$

$$Dpf := \begin{bmatrix} [0.00059599999999999960 + 0. I, \\ 0.000129499999999999978 - 0.0000464766966697648528 I, \\ 0.000129499999999999978 + 0.0000464766966697648528 I], [\\ 0.0000284999999999999508 - 0.0000256920869789383448 I, \\ 0.0000110000000000000030 - 0.0000167431578064991528 I, \\ 0.000017499999999999918 - 0.00000779422863405995740 \\ I], [\\ 0.0000284999999999999508 + 0.0000256920869789383448 I, \\ 0.000017499999999999918 \\ + 0.00000779422863405995740 I, \\ 0.0000110000000000000030 + 0.0000167431578064991528 I] \\] \end{bmatrix}$$

> $gpf2 := MatrixInverse(gpf)$

$$gpf2 := \begin{bmatrix} [3915.07910881499493 + 0. I, \\ 40432.2731675818504 - 66139.1831420513627 I, \\ 40432.2731675817559 + 66139.1831420514354 I], [\\ -1876.81627381336148 - 9123.04772310866975 I, \\ -3.82265095253473264 \cdot 10^5 - 2.48512752089635382 \cdot 10^5 I, \\ 3.84737245721668588 \cdot 10^5 - 2.70260093820391339 \cdot 10^5 I], [\\ -1876.81627381336876 + 9123.04772310866975 I, \\ 3.84737245721668180 \cdot 10^5 + 2.70260093820391805 \cdot 10^5 I, \\ -3.82265095253473614 \cdot 10^5 + 2.48512752089634888 \cdot 10^5 I] \\] \end{bmatrix}$$

> $Id2 := ((gpf \cdot gpf2) \cdot gpf) - gpf$

$$\begin{aligned}
 Id2 := & \left[\right. \\
 & 1.08420217248550444 \cdot 10^{-19} - 1.56072732726740794 \cdot 10^{-18} I, \\
 & -2.43945488809238499 \cdot 10^{-19} \\
 & - 9.21571846612678769 \cdot 10^{-19} I, \\
 & 0. - 9.08019319456609964 \cdot 10^{-19} I], [\\
 & 1.21972744404619249 \cdot 10^{-19} + 1.96511643762997680 \cdot 10^{-19} I, \\
 & -6.77626357803440272 \cdot 10^{-21} \\
 & + 1.82959116606928874 \cdot 10^{-19} I, \\
 & -3.38813178901720136 \cdot 10^{-20} \\
 & + 2.06676039130049284 \cdot 10^{-19} I], [\\
 & 2.84603070277444916 \cdot 10^{-19} + 2.71050543121376109 \cdot 10^{-20} I, \\
 & 1.08420217248550444 \cdot 10^{-19} - 9.14795583034644366 \cdot 10^{-20} I, \\
 & 9.48676900924816380 \cdot 10^{-20} - 4.74338450462408190 \cdot 10^{-20} I] \\
 & \left. \right]
 \end{aligned}$$

> $Dtf := (gtf.gpf2).Dpf$

$$\begin{aligned}
 Dtf := & \left[\right. \\
 & 0.0000302958307770961584 - 2.20228566286118088 \cdot 10^{-20} I, \\
 & 0.00000696372733021204512 - \\
 & \quad 0.00000220338613559913197 I, \\
 & 0.00000696372733021205106 \\
 & \quad + 0.00000220338613559911926 I], [\\
 & 0.00000278433154396728488 - \\
 & \quad 0.00000217245970290189496 I, \\
 & 0.00000150322876305026940 - \\
 & \quad 0.00000164507280076274146 I, \\
 & 0.00000187342370977289434 - 9.55348255232040664 \cdot 10^{-7} I], \\
 & [\\
 & 0.00000278433154396731284 \\
 & \quad + 0.00000217245970290193052 I, \\
 & 0.00000187342370977291044 + 9.55348255232054218 \cdot 10^{-7} I, \\
 & 0.00000150322876305027618 \\
 & \quad + 0.00000164507280076276264 I] \left. \right]
 \end{aligned}$$

> $Dt := \text{InverseFourierTransform}(Dtf)$

$$Dt := \begin{bmatrix} 0.0000188484178237004020 + 1.18584612615602048 \cdot 10^{-20} \text{ I}, \\ 0.0000101783762512108648 + 1.81768249650878491 \cdot 10^{-21} \text{ I}, \\ 0.00000683769979011948762 - 1.23616602000184343 \cdot 10^{-22} \text{ I} \\], [\\ 0.0000154430577978689293 - 3.79644470527858292 \cdot 10^{-20} \text{ I}, \\ 0.00000917374273490475164 - 1.80355553124419640 \cdot 10^{-20} \text{ I}, \\ 0.00000665750928317727818 - 8.07889314867078206 \cdot 10^{-21} \text{ I} \\], [\\ 0.00000993180981595092414 - 8.62236504620068946 \cdot 10^{-21} \text{ I}, \\ 0.00000779636119631902212 - 4.58710105942377446 \cdot 10^{-21} \text{ I}, \\ 0.00000602051763803680869 - 2.33273542238119123 \cdot 10^{-21} \text{ I} \\] \end{bmatrix}$$

>

b5					
	A	B	C	D	E
1	0.0000 + 1.18\ 6 10 ⁻²⁰ I	0.0000 + 1.81\ 8 10 ⁻²¹ I	0.00000 - 1.23\ 6 10 ⁻²² I		
2	0.0000 - 3.79\ 6 10 ⁻²⁰ I	0.00000 - 1.80\ 4 10 ⁻²⁰ I	0.00000 - 8.07\ 9 10 ⁻²¹ I		

3	0.00000 — 8.62\ 2 10 ⁻²¹ I	0.00000 — 4.58\ 7 10 ⁻²¹ I	0.00000 — 2.33\ 3 10 ⁻²¹ I		
4					
5					

InsertMatrixIntoSelection(b5,Dt)

Warning, inserted missing semicolon at end of statement

>

VITA

Jabari Robinson was born on January 13, 1981, in Baton Rouge, Louisiana. He graduated from Southern University & A&M College in 2003 with a Bachelor of Science in physics. During his time at Southern University he was involved in a publication, “Direct conversion of TiO_2 sol to nanocrystalline anatase at 85°C ”, that was accepted by the *Journal of Materials Research*. In December 2006, he is expected to graduate from Louisiana State University with a Master of Science in medical physics and health physics.